

Available online at [www.sciencedirect.com](http://www.sciencedirect.com)

**jmr&t**  
Journal of Materials Research and Technology  
journal homepage: [www.elsevier.com/locate/jmrt](http://www.elsevier.com/locate/jmrt)



## Original Article

# Microstructure dependent electroplastic effect in AA 6063 alloy and its nanocomposites



Jai Tiwari <sup>a</sup>, Padma Pratheesh <sup>a,1</sup>, O.B. Bembalge <sup>a</sup>,  
Hariharan Krishnaswamy <sup>a,\*</sup>, Murugaiyan Amirthalingam <sup>b</sup>,  
S.K. Panigrahi <sup>a</sup>

<sup>a</sup> Manufacturing Engineering Section, Department of Mechanical Engineering, IIT, Madras, Chennai, 600036, India

<sup>b</sup> Department of Metallurgical and Materials Engineering, Indian Institute of Technology Madras, Chennai, 600036, India

## ARTICLE INFO

## Article history:

Received 8 January 2021

Accepted 29 March 2021

Available online 9 April 2021

## Keywords:

AA 6063

Electric-assisted deformation

Joule heating

Electroplastic effect

Dislocation density

X-ray diffraction

## ABSTRACT

The flow stress reduction during plastic deformation superposed with electric current, commonly referred as ‘electroplasticity’ has been actively researched over the past few decades. While the existence of an electron–dislocation interaction, independent of Joule heating is established, the exact rate controlling mechanism of the observed behaviour lacks consensus. Understanding the governing mechanism is complex due to the combined effect of Joule heating and electron–dislocation interaction. The present work attempts to establish the electroplastic mechanism in AA 6063 alloy and its nanocomposites. The role of microstructure on the electron interaction is investigated by preparing four distinct microstructure from the base alloy. All the samples were subjected to constant amplitude direct current during plastic deformation. The Joule heating effect is decoupled using the experimentally measured temperature history. The potential electroplastic mechanism for the alloy is elucidated by analysing the trend of flow stress reduction with strain and strain rate. It is inferred that micro Joule heating and electron wind effect cannot completely explain the observed electroplastic behaviour in AA 6063. The SiC particles in nano-composites suppressed the electroplastic effect.

The observed mechanical behaviour under electric current is in agreement with the trend predicted assuming magnetic depinning mechanism. The reduction of dislocation density quantified using X-ray diffraction is found to concur with the inferred mechanism.

© 2021 The Author(s). Published by Elsevier B.V. This is an open access article under the CC BY-NC-ND license (<http://creativecommons.org/licenses/by-nc-nd/4.0/>).

## 1. Introduction

Electric-assisted forming (EAF) is known to improve the room temperature formability of engineering alloys and metal

matrix composites. As the name suggests, the process involves simultaneous application of electric current during plastic deformation. The complex interaction between the applied current and plastic deformation on the mechanical behaviour is generally referred as electro-plastic effect.

\* Corresponding author.

E-mail address: [hariharan@iitm.ac.in](mailto:hariharan@iitm.ac.in) (H. Krishnaswamy).

<sup>1</sup> presently working with Larsen & Toubro.

<https://doi.org/10.1016/j.jmrt.2021.03.112>

2238-7854/© 2021 The Author(s). Published by Elsevier B.V. This is an open access article under the CC BY-NC-ND license (<http://creativecommons.org/licenses/by-nc-nd/4.0/>).

Increasing the deformation temperature<sup>2</sup> by partial or complete heating of the work piece, referred to as warm forming is a well-known solution to improve the formability of difficult to form alloys [1,2]. Warm forming or intermediate annealing involves large heating furnaces for heating the component and is time-intensive. The EAF technique on the other hand can improve the formability at reduced costs, energy and time when compared to warm forming.

The earliest reported work on interaction of electrons and dislocations can be traced back to 1960s on the study of superconductivity [3,4]. The reduction of flow stress due to the absence of electron drag on moving dislocations were used to analyze the superconductivity in metals [5–7]. Theoretical considerations developed then were used later to understand the electroplastic mechanism. The use of this interaction to aid plastic deformation, however can be attributed to the subsequent work of Troitskii and Likhhtman [8] who coined the term “Electroplastic effect”. It was initially believed that the changes observed in the mechanical behaviour of materials with the application of current were primarily due to the associated Joule heating [9,10]. However, subsequent efforts [6,11,12] in this field proved that this effect can be observed even under isothermal conditions [13]. In regards to changes in mechanical behaviour, researchers [14–18] have established that application of current pulses during plastic deformation considerably reduces the flow stress and increases the ductility in the material. Application of current pulses significantly reduces the material hardness, when compared to other furnace thermal treatments [19]. In addition to that, springback reduces, as demonstrated for AZ31B sheets [20] in electric assisted V-bending test. Complete elimination of springback was demonstrated [21] in Al 6111 sheet specimen with the application of high amplitude and short duration current pulses. Also, reduction in anisotropy effects of Al 5083 was noticed when constant DC is passed through the specimen while deforming the material [22].

The role of electric pulses on mechanical behaviour of the composites [23] and bulk metallic glasses [24–26] is investigated in detail to understand (i) electroplastic effect [12] (ii) electromigration effect [27] (iii) recrystallization behaviour and (iv) deformation behaviour occurring at atomic scales. These studies primarily conclude that the athermal effect induced by electropulsing dominate the observed changes in mechanical properties. The effectiveness of electrically assisted deformation is closely linked to the microstructure of the material. Experimental results [28,29] indicate that fine grained structures exhibit an increased electroplastic effect. Similarly, greater mobility of grain boundaries during electropulsing treatment of nickel based superalloy is reported by Zhang et al. [30]. Kim et al. [31] compared the mechanical behaviour of Al5052–H32 (as-received and 30% cold-rolled) under a pulsed electric current. They concluded that in the presence of electric current, the samples tend to anneal at a temperature less than the critical annealing temperature of the alloy, suggesting a distinct electron–dislocation interaction mechanism apart from Joule heating. Dislocation evolution captured using the in-situ transmission electron microscopy during the electrically-assisted manufacturing

of Inconel 718 further strengthens the independent electron–dislocation interaction viewpoint [32]. Observations of grain boundary melting and cavitation in brass alloys, well below their melting point under the influence of electric current is reported by Fan et al. [33]. These observations can be linked to non-homogeneous temperature distribution due to sub-structure variation leading to increased heating at the grain boundaries. Along with a decrease in recrystallization temperature, homogenization of various texture was observed in cold rolled Fe-3% Si alloy strip due to application of pulsed current. Recrystallization at a lower temperature near to the fracture surface was reported for 316L stainless steel, when electrical pulses were applied during the tensile test [34]. Formations of new nano phases [35] were observed, when the Cu–Zn alloy was subjected to electropulsing. It was demonstrated that even static electropulsing preceding cold deformation enhanced the ductility of Zn–Al alloy [36] due to reduction in internal residual stress and microstructural changes. In general, the effect of electric current follows a threshold phenomenon [28,37–39] below which electroplastic effect is insignificant.

The simplest explanation for the observation of electroplastic behaviour is the associated Joule heating. A significant part of research has been devoted to justify that there exists an additional independent mechanism related to interaction between moving electrons and dislocations [13,14]. While the existence of such independent mechanism is generally not disputed, decoupling the contribution of Joule heating and other similar effects still remain as a challenge. In an initial attempt, Okazaki et al. [13] proposed an interesting indirect test to correlate the temperature rise with the change in elastic modulus. They concluded that around 40–70% of total stress drop is due to Joule heating. They also showed that the secondary effects such as skin and pinch effects on the electric current induced stress drop is negligible. With the development of thermographic inspection over the past decades, direct measurement of temperature in the deforming sample has relatively become simpler. Assuming the principle of superposition for the stress drop, finite element studies have also been utilized to separate the Joule heating effects [40–43]. Interestingly, the conclusions were not significantly different from the earlier studies [12,13] without the use of such sophisticated direct measurements. By subtracting the contribution of thermal effect, the stress drop purely due to electroplastic effect can be decoupled from the experimental results.

Troitskii and co-workers [8,44] attributed the electroplastic effect to the momentum transfer between moving electrons and dislocations during scattering [38,45] and is referred as “electron wind effect”. Theoretical considerations [5–7] show that the dynamic force exerted by the electron wind on dislocations is proportional to the difference between the drift velocity of electrons  $v_e$ , and the dislocation velocity  $v_d$ . If  $v_e < v_d$ , the electrons decelerates the moving dislocations due to electron drag. Thus, electron wind effect can easily explain the occurrence of threshold current density above which electroplastic effects can be sensed. Systematic studies [12,46–48] on electroplastic effect concluded that the electron wind mechanism had a relatively smaller contribution to the total stress drop. According to electron wind effect, the stress

<sup>2</sup> well within the recrystallization temperature.

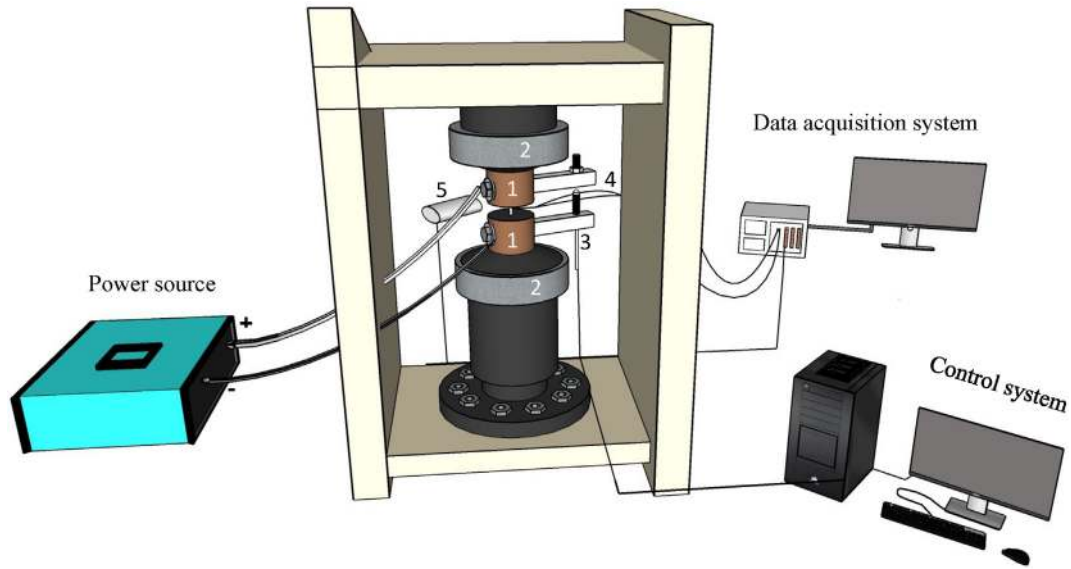


**Fig. 1 – Schematic diagram of electrically assisted compression setup used in the present work. In figure, marked components are: (1) Steel platens with electric cable connections from the power source (2) Syndanio insulation (3) LVDT (4) Thermocouple wire wrapped around the specimen and (5) Infrared sensor placed nearby specimen. The components (4) and (5) were connected with data acquisition system to measure the temperature during the deformation. Force and position measurements were recorded using the control system unit of the setup.**

drop is attributed to the change in thermal component of flow stress, which is accounted in the activation energy ( $\Delta G$ ) of plastic strain rate,  $\dot{\epsilon} \propto \exp(-\Delta G/kT)$ . While the thermal component varied linearly with current density ( $J$ ), the proportionality constant or pre-exponential factor in  $\dot{\epsilon}$  increased with  $J^2$ , suggesting a relatively smaller contribution of electron wind effect [12]. In the same period, Klimov et al. [6] critically analyzed the existence of an independent electroplastic effect and suggested that heterogeneity of temperature distribution throughout the lattices of a material leads to micro-Joule heating in addition to the macro level Joule heating present in the material. Researchers [6,49,50] in the past, have argued that the combined micro and the macro-Joule heating is the main contributor to the observed electroplastic effect. It was shown by Lee et al. [20,43] and Jones et al. [41] that the numerical prediction of temperature rise during electropulsing of AZ31 alloy correlates with the experiments when 100% of the electrical energy is converted to heat. Their results supported Joule heating (micro and macro) mechanism to be responsible for the observed electroplastic effect. In a related work [51], it was shown that the heterogeneous heating especially at microcrack tips can facilitate reorganization of defect structure inside the material.

Molotskii and Fleurov [52] proposed an alternative mechanism of magnetoplasticity to explain the electroplastic behaviour. According to them, magnetic field induced by the

applied current leads to depinning of dislocations from the paramagnetic obstacles. In a recent work, Lahiri et al. [53] using crystal plasticity finite element simulations analyzed the relative contribution of electron wind effect, thermal softening and magnetic depinning of dislocations during electrically-assisted deformation. They have concluded that magnetoplasticity based mechanism is the dominant one among all the mechanisms considered. Conrad [38] pointed out that the magnetoplasticity can be accounted in the pre-exponential factor of electron wind model. Similarly, attempts [45,54] to modify the function of ' $J$ ' in the expression of  $\Delta G$  provides a comprehensive explanation for electron wind effect. Albeit the considerable past work [55], the governing mechanism for electroplasticity is not established till date.

Accounting the electroplastic phenomenon in a constitutive relationship is essential to model the electric assisted forming process. Attempts have been made to modify the empirical stress–strain relations such as Hollomon hardening [56] or Johnson–Cook model [57] to include the electric assisted plastic deformation. Wang et al. [58] proposed an analytical flow stress model for AZ31 alloy superposing different rate dependent mechanisms that influence electroplasticity. They modelled the effect of electric current in thermal softening, strain hardening by solute dislocation interaction and electron wind effect. Hariharan et al. [59] proposed a dislocation density based hardening model to account the electroplastic effect. The rate dependent parameters of the dislocation density model were extended to include the dependence of electrical current density. Recently, Dimitrov et al. [60] proposed a more generic multiphysics internal state variable model to couple the electro-mechanical behaviour. In general, the constitutive models attempt to modify the rate dependent and rate independent terms phenomenologically to account for the electrical effect. The mathematical form of the

<sup>3</sup> Cryorolling refers to cold rolling at extremely low temperature. The process inhibits dynamic recovery and results in grain refinement. In practice, samples soaked in liquid nitrogen are rolled quickly before the temperature raises to room temperature. In the present work, 110 mm diameter roll at a speed of 8 rpm in a mill is used for this process. Between each successive pass, the samples are soaked in liquid nitrogen for 10 min to achieve constant temperature.

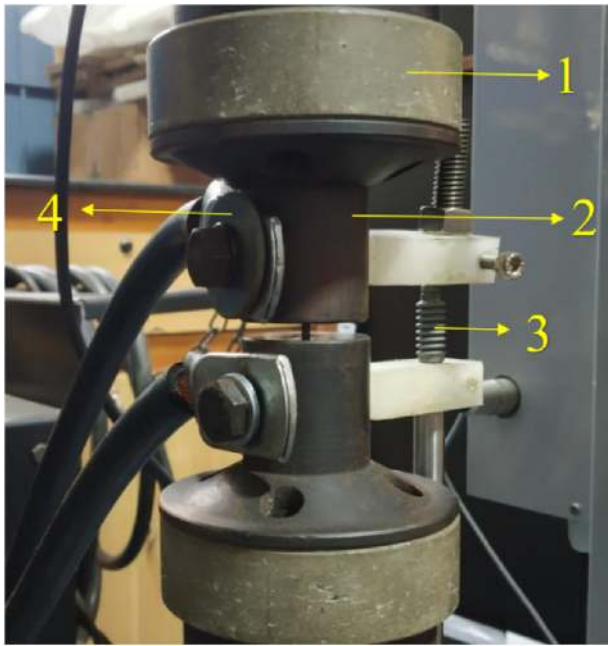


**Fig. 2 – Electrically assisted compression setup used in the present work: (1) Syndanio insulation (2) Steel platens (3) LVDT and (4) Electric cable connections from power source.**

phenomenological relation depends upon the underlying electroplastic mechanism assumed in the model. The essential validation of any constitutive electroplastic model is the dependence of flow stress on the applied current density, which require experimental data over a wide range of applied current density.

It can therefore be summarized that the lacuna in the understanding of electroplasticity phenomena can be addressed by (i) establishing the fundamental governing mechanism over a range of materials and (ii) developing experimental data to formulate reliable constitutive models. The present work is an attempt to advance the understanding of underlying mechanism in AA 6063 alloy. Although the mechanism of electroplasticity is still not clear, it is well established that the effect of current over the material is closely related to microstructure. Therefore, AA 6063 alloy with four different microstructures was chosen to understand the electroplastic behaviour during uniaxial compression. Most of the past work utilized pulsed current to improve the ductility. Since the focus of the present work is to understand the influence of the electrical current on flow stress evolution, experiments were carried out using a constant amplitude direct current. The experimentally measured temperature history was utilized to decouple the Joule heating effect. X-ray diffraction analysis was carried out on the deformed samples to correlate the dislocation densities with the electroplastic behaviour. In the present work, the X-ray diffraction studies are used to quantify the change in dislocation density. While this could be influenced by residual stress [61], the result could be only a secondary effect and cannot be attributed solely due to residual stress. On the other hand, the reduction in springback can be related to residual stresses. The outcome of the present work indicates that the governing mechanism of electroplastic deformation

**Table 1 – Chemical composition of the AA 6063 alloy used in this work.**

Elements	Mg	Si	Cr	Cu	Fe	Mn	Zn	Ti	Al
Weight %	0.89	0.54	0.08	0.09	0.22	0.031	0.08	0.01	Balance

in the chosen material is the magnetic depinning of paramagnetic obstacles.

## 2. Methodology

The test set up used for performing electric assisted forming (EAF) experiments is shown in Figs. 1 and 2. Owing to its wider applications [62,63], AA 6063 alloy was chosen for the present work. The chemical composition of the alloy is given in Table 1.

The AA 6063 alloy was subjected to appropriate thermo-mechanical processing and heat treatment to study the influence of microstructure on the electroplastic effect. Samples containing four variants in microstructural constituents were obtained and the details of these samples are summarised below. In the subsequent sections, the acronym within the braces is used for brevity.

1. AA 6063 alloy with solution treatment and room temperature aged (STA)
2. AA 6063 alloy in 70% cold worked condition (CW),
3. AA 6063 alloy with silicon carbide as nano-composite material (NC),
4. AA 6063 alloy with silicon carbide as nano-composite material in 70% cold worked condition (NC + CW).

AA 6063 alloy samples of 11 mm thickness were cast and partially rolled (from 11 mm to 10 mm thickness) at room temperature to reduce the porosity. The compression samples were machined to a thickness of 3.5 mm and solution treated at 530 °C for 2 h followed by iced water quenching. These samples were then aged (STA) for a period of 15 days at room temperature. The cold worked microstructure, CW was achieved by cryorolling<sup>3</sup> the AA 6063 plates of 10 mm thickness.

The nano-composite (NC) samples were produced by stir casting AA 6063 alloy with 4 wt. % of SiC as reinforcement. To prepare the NC samples, AA6063 alloy blocks were molten in the furnace at a temperature of 700 °C. The melt was stirred using a Stirrer at 600 rpm for 15 min to ensure proper mixing of reinforcement in the base alloy. The nano (45 nm) sized SiC powder wrapped in aluminum foil were preheated at 600 °C and added into the semisolid vortex through mechanical stirring. Subsequently, the material was solution treated at a temperature of 535 °C for 2 h followed by iced water quenching. The NC samples were further cryorolled (NC + CW) to induce work hardening and uniformly distribute the SiC reinforcement particles into the matrix.

### 2.1. Electroplasticity experiments

Cylindrical specimens of 2 mm diameter and 3.4 mm length (L/D ratio = 1.7, where L and D refer to length and diameter of

**Table 2 – Experimental parameters used in the present work.**

Sl. No.	Initial current density (A/mm <sup>2</sup> )	Cross-head velocity (mm min <sup>-1</sup> )	Initial strain rate (s <sup>-1</sup> )
1	0	0.50	2.5*10 <sup>-3</sup>
2	0	1.00	5.0*10 <sup>-3</sup>
3	0	1.50	7.5*10 <sup>-3</sup>
4	19.45	0.50	2.5*10 <sup>-3</sup>
5	19.45	1.00	5.0*10 <sup>-3</sup>
6	19.45	1.50	7.5*10 <sup>-3</sup>

the specimen respectively.) were wire cut to size as per ASTM-E9 standard. Standard polishing method using a series of emery papers was used to grind the specimen and to remove the surface oxides formed during heat treatment. A 10 kN hydraulic Universal Testing Machine (UTM) was used to perform the electrically assisted compression experiments. The constant amplitude direct current was supplied by a commercially available welding power source (Miller Dynasty 200 DX). A specialized compression fixture (Fig. 1) was used for the electrically assisted compression test to connect the cables from the power source. The compression fixture consisted of hardened steel platen and a suitable 'Syndanio' insulation sheet that can insulate the electrical current till 350 °C. The displacement and force data of the deforming sample were continuously recorded in the control system unit of the UTM. A preload of 50 N was applied to the specimen to ensure sufficient initial contact between the platens and specimen. Series of monotonic compression tests were performed (Table 2) at room temperature (around 27 °C).

The electrically-assisted compression tests were carried out with a constant amplitude direct current of 61 A (current density  $\approx 19.45 \text{ Amm}^{-2}$ ) throughout the deformation. To verify the repeatability of results, all the experiments were performed at least three times. The electric current supplied was measured using a MECO TRUE RMS clamp meter. The specimens were deformed within the strain rate range of  $2.5 * 10^{-3} - 7.5 * 10^{-3} \text{ s}^{-1}$  up to a strain of 15%.

The associated Joule heating due to application of electric current increases the temperature of the sample. The temperature change during the electrically assisted deformation was continuously measured using a Texense IFbN-1200 Infrared (IR) fiber optical non-contact temperature sensor. The response time of this sensor was less than 5  $\mu\text{s}$  and the sensor could measure a temperature range of 0–1200 °C. Initially, the temperature evolution in selected samples were measured using both IR sensor and a K-type thermocouple to calibrate the IR sensor. Since the size of the selected specimens were very small, welding of the thermocouple on the specimen was not considered. Instead, the thermocouple wires were tightly wrapped around the specimen as shown in Fig. 1, so that they do not loose contact during the deformation. The thermocouple wires were connected to the NI PXIe-1071 Data Acquisition (DAQ) System, which records the temperature variation at a frequent of 2 Hz. Non-contact type IR sensor was placed near the specimen such that specimen and the sensor fall in a straight line horizontally (Fig. 1). The fiber optical sensor was connected to the NI Data Acquisition system to record the temperature change throughout the deformation process.

Uniaxial high-temperature isothermal tests were performed using Instron universal testing machine (UTM-5948). All the four materials were tested at temperatures 100 °C and 200 °C, at a constant strain rate of  $7.5 * 10^{-3} \text{ s}^{-1}$ . The samples along with the gripper were preheated and soaked at test temperature for 30 min before the test. The inbuilt load cell and extensometer were used to record the force and displacement, respectively during the test.

The interaction between the substructure and applied current were studied by diffraction experiments. X-ray diffraction analysis on samples deformed with and without the application of electric current was performed using Cu-K $\alpha$  radiation in a Bruker AXS D8 Discover X-ray diffractometer. The correction in the instrumental broadening was done using a suitable aluminium standard.

It should be noted that the sample preparation process including the edge polishing influences the surface roughness of the sample. The edge quality can influence the accuracy of the measured physical quantity. While the effect on tensile strength is found [64] to be within acceptable limits, its effect on electric charge storage is not investigated. The local charge density can affect the skin effect, which is generally negligible. The local variation in electric charge density can influence the crack initiation mechanism [65]. Understanding the role of sample preparation or the effect of testing machine [66], though important is beyond the scope of the present work. If such effects are significant, hybrid microstructure based models has to be incorporated [67] to account for the electrical effect.

### 3. Results

The solution treatment ensures homogeneity in chemical composition and complete dissolution of precipitates as compared to the as-cast material. In general, the strength ( $\sigma$ ) due to different strengthening mechanisms can be linearly superposed as [68].

$$\sigma = \sigma_{\rho} + \sigma_{\text{GB}} + \sigma_{\alpha} + \sigma_{\gamma} + \dots \quad (1)$$

where, the subscript ' $\rho$ ', 'GB', ' $\alpha$ ' and ' $\gamma$ ' refers to dislocation density, grain boundary, solutes and precipitates respectively. The initial strength in STA is primarily due to resistance offered by grain boundary and dislocation pinning [69] by solute atoms. The STA sample exhibits significant work hardening with deformation due to dislocation multiplication. Increase in dislocation density during cryorolling led to higher initial strength of the 'CW' sample. The rate of work hardening in CW is however less than that of STA, evident from the slope of stress–strain curve (Fig. 3a).

The dispersion of SiC nano-particles in NC sample provides resistance to dislocation motion and thereby increases the strength compared to solutionized<sup>4</sup> samples [70]. The strain

<sup>4</sup> The solutionized here does not refer to the aged (STA) samples. As indicated in section 2 solutionized samples were aged in the present study. The aged solution treated (STA) samples are found to be stronger than (Fig. 3a and b) nano-composites (NC) due to the difference in ageing kinetics, which is beyond the scope of present investigation.

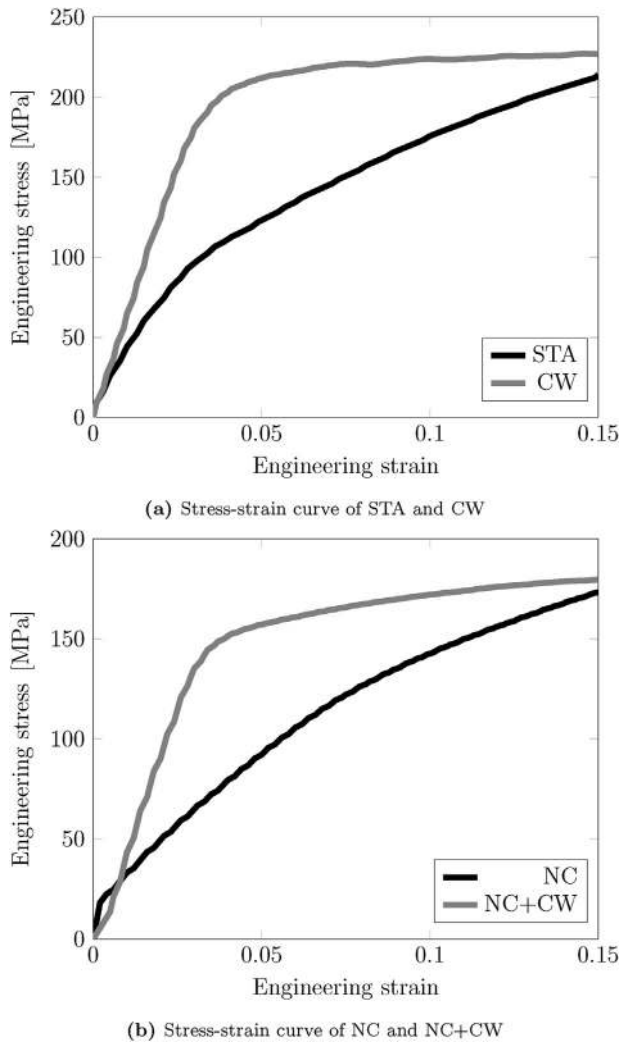


**Fig. 3 – Engineering stress–strain behaviour in uniaxial compression is plotted up to 15% of engineering strain for all four microstructural conditions in AA 6063. Stress–strain behaviour of solutionized condition in base alloy as well as its composite is shown in black. Whereas, stress–strain behaviour of cold worked condition in base alloy and its composites is represented by gray line.**

gradient due to differential coefficients of thermal expansion (CTE) of SiC and AA 6063 during solution treatment and ageing leads to increase in geometrically necessary dislocation (GND). These GNDs are inversely proportional to the size of SiC particles [70]. Therefore the strengthening in NC sample is due to the combined effect of grain boundary strengthening and dislocation strengthening. The Orowan mechanism of dislocation looping around SiC particles due to cold working, in addition to other mechanisms including ultrafine grain structure contributes to higher strength in NC + CW samples [70].

All the mechanical tests (with and without external current) were conducted up to 15% of engineering strain to avoid potential shear fracture. The initial yield strength of STA sample is approximately 95 MPa. Noticeable increase in yield strength is observed in CW condition, as demonstrated in Fig. 3a. Similar observations are recorded in case of NC and NC + CW as shown

in Fig. 3b. The increased strength and reduced work hardening in the cold worked state (both CW and NC + CW) are in accordance with the expected mechanical behaviour where the large plastic strain and suppressed dynamic recovery has led to significant increase in dislocation density.

The flow stress decreased in all the cases when the deformation proceeded in the presence of electric current (Fig. 4a–d). The reduction in flow stress is due to the superposition of electroplastic and thermal (Joule heating) effect. In STA, the observed stress drop gradually increased and saturated with strain. The stress drop is higher in the case of NC with respect to STA. The stress drop in the cold worked condition (CW) is much higher than that of the STA whereas NC + CW is in the similar order of NC. The results comparing the flow stress curve of with and without current-assisted AA6063 specimens are shown in Fig. 4a–d respectively. It is interesting to note that the drop in flow stress ( $\Delta\sigma$ ) due to electrical assisted deformation is strongly influenced by the initial microstructure. While the flow stress difference increased with strain in STA and NC, reverse trend is noted in CW and NC + CW samples.

The baseline (without external current) and EA tests are conducted at three different strain rates. From the results, it is evident that the baseline tests showed negligible strain rate dependence, whereas EA tests depend strongly on strain rate. The flow stress difference between EA test and monotonic test ( $\Delta\sigma$ ) vs true plastic strain ( $\epsilon_p$ ) in STA samples is plotted for different strain rates in Fig. 5. It is observed that the electroplastic effect is strongly dependent on both strain and strain rate. Similar strain rate dependence is observed in other material samples too. These results in Fig. 5 however includes the thermal effect on the flow stress due to Joule heating. The temperature history during EA test is recorded to decouple the Joule heat effect from the experiments. As mentioned in the previous section, IR optical sensor is used for temperature measurement. In selected cases, temperature during EA test is measured simultaneously using both IR sensor and thermocouple. Representative results comparing the outcome of IR sensor and thermocouple plotted in Fig. 6. Very good correlation exists between the IR sensor and thermocouple, as shown in Fig. 6 and other similar tests performed using different material condition. The temperature data obtained using IR sensor in all the cases is used for further analysis. The diffraction pattern obtained from XRD analysis after correction for instrument broadening using a suitable aluminum standard is shown in Fig. 7. The XRD pattern before and after plastic deformation is indicated. The effect of electrical assisted deformation on the diffraction pattern is superposed on the same image.

#### 4. Discussion

The material softening due to electrical effect summarized in previous section indicates that the flow stress reduction is strain dependent. The flow stress drop ( $\Delta\sigma$ ) in STA and NC samples increased with strain. However reverse trend is observed (Fig. 4a–d) in both the cold worked conditions. The effect of electricity seems to diminish with increasing strain rate irrespective of the microstructure. The effect of electric

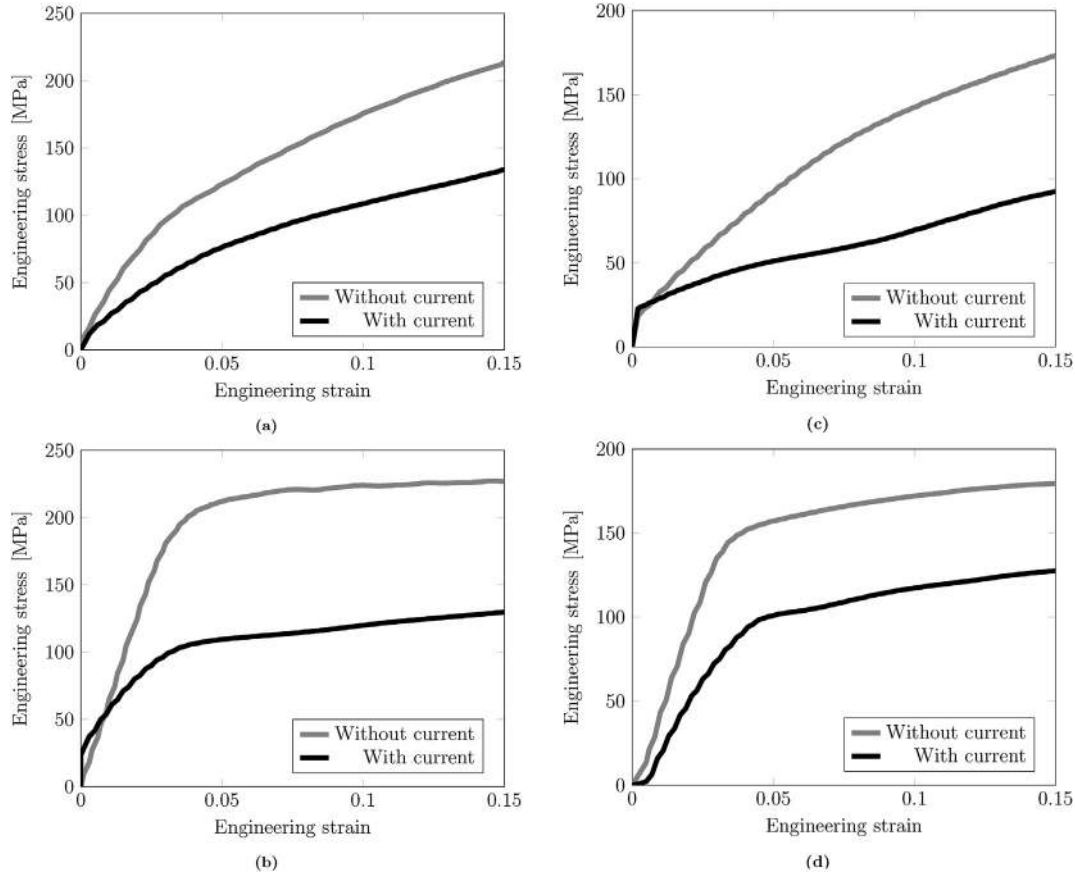


**Fig. 4 – Engineering stress–strain behaviour of monotonic and electric assisted compression is compared up to 15% of engineering strain in following order of four microstructural condition of AA6063 specimens (a) STA, (b) CW, (c) NC and (d) NC + CW. Flow stress curves of without current condition are shown in gray whereas with current condition are represented by black lines.**

current on flow stress reduction is maximum in case of least strain rate following the trend reported in literature [39,71].

Although, Figs. 4a–d and 5 are indicative of reduction in flow stress during EA compression, the softening cannot be purely attributed to electrical effect. The net reduction in flow stress is due to superposition of (a) Electron-dislocation interaction (b) Thermal effect and (c) Pinch effect. Since direct current is utilized for electrical assisted deformation, the skin effect can be ignored. The pinch pressure  $P$  due to flow of current can be calculated as [12,13]:

$$P = \frac{1}{4} \mu J^2 (r_0^2 - r^2) \quad (2)$$

where,  $\mu$  represents the magnetic permeability of the material,  $J$  is the applied current density,  $r_0$  and  $r$  refer to the radius of the sample and distance from the center of the sample, respectively. This pinch pressure reduces the effective stress during deformation. The decrease in stress due to pinch effect ( $\Delta \sigma_{pinch}$ ) is given by [13].

$$\Delta \sigma_{pinch} = 2\nu P \quad (3)$$

where,  $\nu$  is the Poisson's ratio.

Assuming  $\mu = 12.57 \cdot 10^{-7} \text{ N A}^{-2}$  [72], the maximum pinch pressure (at the center of the sample,  $r = 0$ ) is estimated (eq. (2)) to be  $1.2 \cdot 10^{-4} \text{ MPa}$ . The corresponding stress drop from eq. (3) is  $7.8 \cdot 10^{-5} \text{ MPa}$ , which is negligible when compared to the total stress drop.

Therefore, the observed flow stress softening is primarily due to electroplastic and thermal effect. The thermal effect here refers to the temperature rise due to Joule heating, that can be quantified as

$$\Delta T = \frac{\eta I^2 R t}{m C_p} \quad (4)$$

where,  $t$  is the time over which external current  $I$  is applied,  $R$ ,  $m$  and  $C_p$  respectively refers to electrical resistance, mass and heat capacity of the material. The efficiency  $\eta$  accounts for the ratio of the input electric power that is converted to heat. The remaining energy  $(1-\eta)^2 R t$  contributes to electroplastic deformation and/or heat loss to environment.

The temperature dependent flow stress decreases with increase in temperature due to Joule heating. Unlike the electropulsing experiments, the thermal expansion due to temperature gradient during pulsing need not be considered in the present experiment with continuous current.

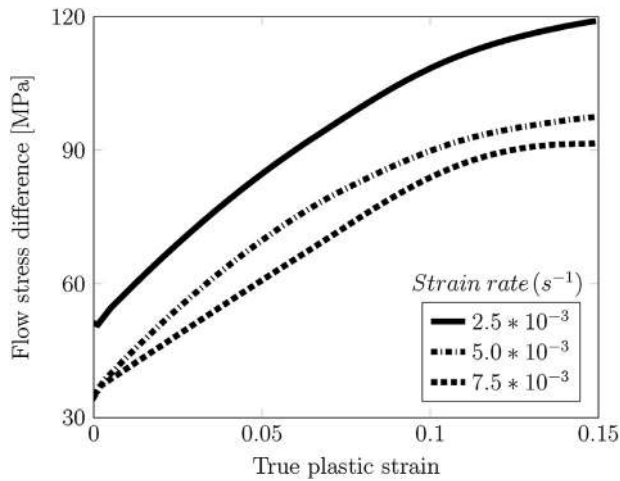


**Fig. 5 – Flow stress difference between monotonic and electric assisted compression tests is plotted with true plastic strain at three different strain rates for STA samples. The stress difference for strain rates of  $2.5 \times 10^{-3}$ ,  $5 \times 10^{-3}$  and  $7.5 \times 10^{-3} \text{ s}^{-1}$  are represented by solid, dashed dot and dashed lines respectively. Flow stress difference ( $\Delta\sigma$ ) is calculated as,  $\Delta\sigma = \Delta\sigma_{\text{monotonic}} - \Delta\sigma_{\text{electrically assisted}}$ .**

Decoupling the contribution of Joule heat effect from the electric assisted experiments is an essential and challenging task in the estimation of electroplastic effect [42].

In the present work, we have attempted to decouple the Joule heating effect by directly measuring the temperature history of the specimens during EA tests.

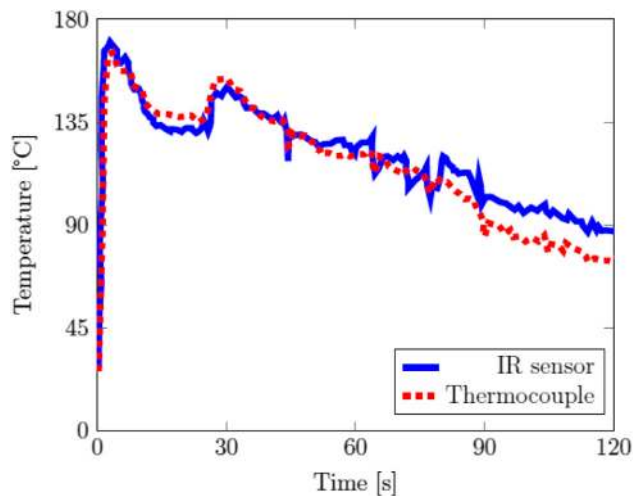


**Fig. 6 – Temperature history during electrical assisted deformation in STA sample indicates good correlation between IR sensor and thermocouple. Temperature measured using IR sensor and thermocouple is represented by gray solid line and black dashed line respectively.**

#### 4.1. Decoupling thermal effect and electroplastic effect

The temperature variation recorded using the IR sensor during electric assisted test is shown in Fig. 8a–d. In general, the temperature drop over a given time interval increases with strain rate. The trend of temperature variation is similar in all the four microstructure, where peak temperature is reached within the first few seconds followed by gradual decrease. The decrease in temperature is due to the heat loss to the environment.

In most of the earlier work [42,43,73,74], the electrical current pulses are applied for very short duration. Assuming adiabatic heat transfer during short duration pulsing, the temperature increase can be estimated from eq. (4). The increase in cross sectional area of the specimen during compression decreases the electrical resistance. On contrary, the resistance increases with temperature [75,76].

When applying constant amplitude direct current such as in the present work, the temperature profile during deformation is complex due to the heat transfer and other temperature dependent material parameters such as electrical resistance and thermal conductivity. In general, the electrical resistance increases with temperature and decreases with the cross sectional area. The cross sectional area increases during compression test leading to drop in electrical resistance (Fig. 9a–d). Under adiabatic condition (ignoring heat transfer to environment), the temperature rises with time leading to increased electrical resistance. Simultaneous transient heat transfer further complicates the temperature history. For instance, if the temperature dependence of electrical resistance is ignored, then the temperature drop with strain (Fig. 9a–d) would be inversely proportional to the strain rate. However, such trend is not observed (Fig. 9a–d) for the above mentioned reasons. Therefore, direct measurement of temperature during electrical assisted experiments (Fig. 8a–d) is used to model the contribution of Joule heating. A less significant yet important aspect is the microstructure dependence of  $\eta$  in eq. (4). Additional experiments are required to correlate  $\eta$  with different material and microstructure.

Isothermal uniaxial tests are performed to estimate the temperature dependent flow stress during deformation and the results are shown in Fig. 10a–d. As expected, the flow stress decreases with increase in temperature. The temperature dependent flow stress during electroplastic deformation at a given strain and strain rate can be calculated by linear interpolation of isothermal stress–strain curve using eq. (5).

$$\sigma_{T,\epsilon} = \sigma_{T_1} + \left[ \frac{\sigma_{T_2} - \sigma_{T_1}}{T_2 - T_1} \right] (T - T_1); T_1 < T < T_2, \quad (5)$$

where,  $\sigma_{T,\epsilon}$  is the temperature dependent flow stress interpolated between experimental values at the given strain ( $\epsilon$ ).  $T_2$  and  $T_1$  are the closest temperature limits.

The contribution of Joule heating during electrical assisted deformation for a given  $\dot{\epsilon}$  can be calculated from eq. (5) as  $\Delta\sigma_{T|\epsilon,\dot{\epsilon}} = [\sigma_{\text{room}} - \sigma_{T|\epsilon,\dot{\epsilon}}]$ . The flow stress reduction due to electroplasticity ( $\Delta\sigma_{ep}$ ) is given as

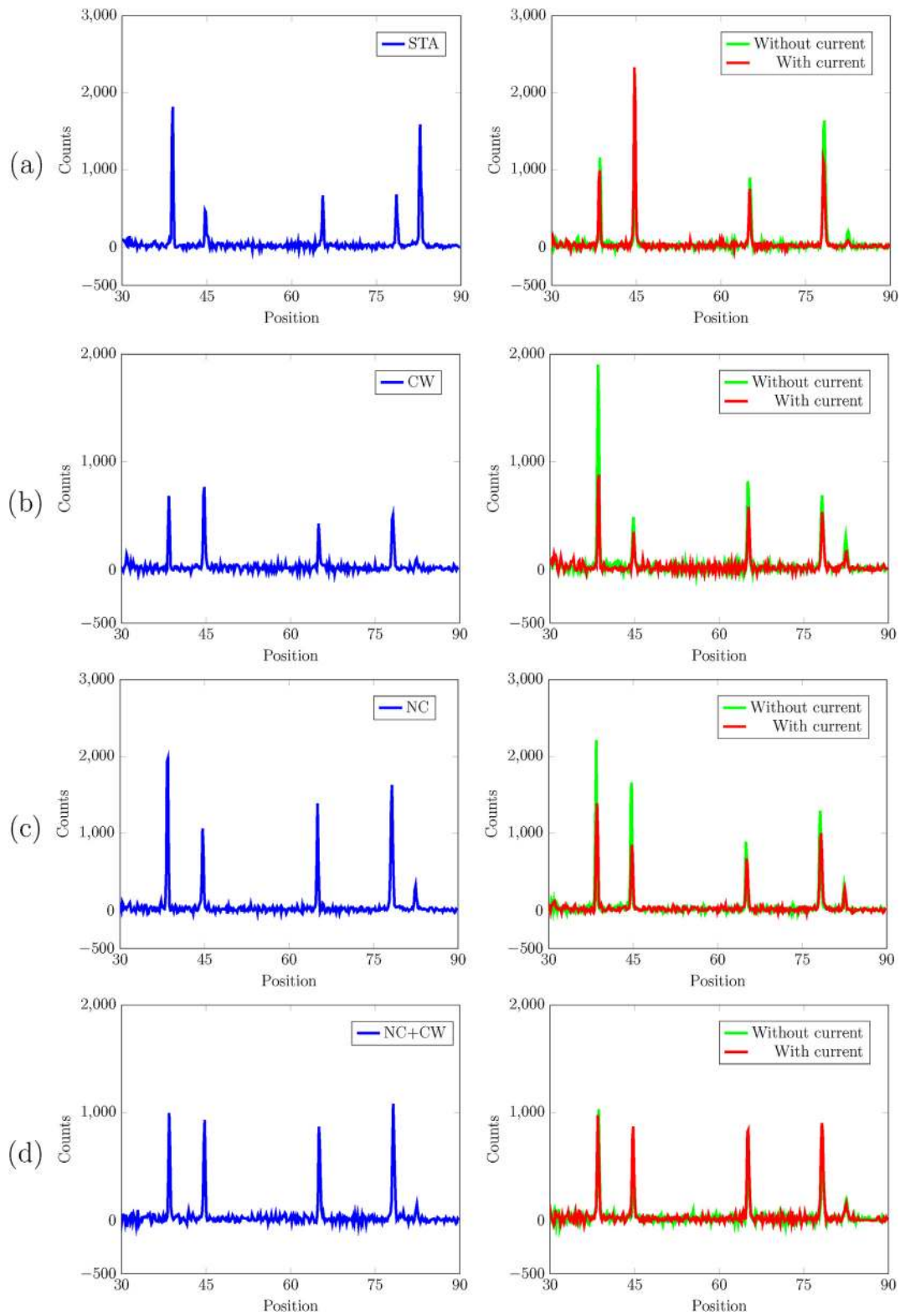


**Fig. 7 – XRD patterns of base material conditions and deformed conditions (with and without current) are presented in following order (a) STA, (b) CW, (c) NC and (d) NC + CW. Blue colour line represents the XRD pattern of base material condition. XRD patterns of deformed condition with and without assistance of current are denoted by red and green colour lines respectively.**

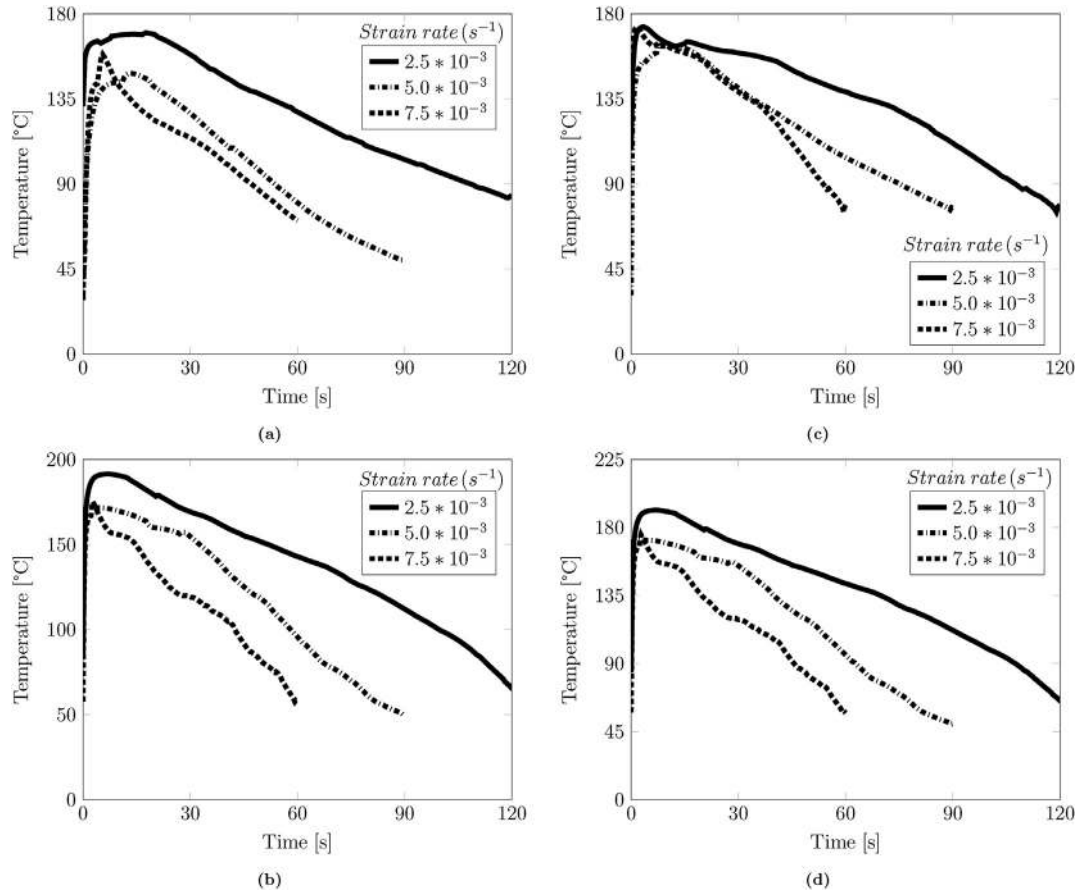


**Fig. 8 – Temperature measurement during electric assisted compression tests at different strain rates is plotted with time for material conditions (a) STA, (b) CW, (c) NC and (d) NC + CW. Temperatures at strain rates of  $2.5 \times 10^{-3}$ ,  $5 \times 10^{-3}$  and  $7.5 \times 10^{-3} \text{ s}^{-1}$  are represented by solid, dashed dot and dashed lines respectively.**

$$\Delta\sigma_{ep} = \Delta\sigma_{exp} - \Delta\sigma_T, \quad (6)$$

where,  $\Delta\sigma_{exp}$  represents the flow stress difference between experimental monotonic and electric assisted test and  $\Delta\sigma_T$  denotes the contribution of Joule heating in total stress drop observed.

The room temperature stress–strain curve with and without electrical assistance is re-plotted in true stress-true plastic strain coordinates. The results for all the four micro-structures are plotted at a strain rate of  $7.5 \times 10^{-3} \text{ s}^{-1}$  for representation purpose in Fig. 11a–d. The effect of varying strain rate over the electroplastic effect ( $\Delta\sigma_{ep}$ ) is considered separately. In Fig. 11a–d, the intermediate curve indicates the effect of Joule heating. The difference between the Joule heating and experimental data quantifies the role of electroplasticity mechanisms.

#### 4.2. Modelling electroplastic effect

A dislocation density based constitutive model proposed by Hariharan et al. [59,77] is used to fit the experimental results. The present model is a generalization of classical Kocks-Mecking-Estrin model [78], according to which flow

stress is modelled as a function of average dislocation density,  $\rho$ .

$$\sigma = M\alpha Gb\sqrt{\rho} \left( \frac{\dot{\epsilon}}{\dot{\epsilon}_0} \right)^{\frac{1}{m}} \quad (7)$$

where,  $M$  is the Taylor factor,  $G$  is the shear modulus (MPa),  $b$  is the Burger's vector (mm) and  $1/m$  is the strain rate exponent.  $\dot{\epsilon}_0$  and  $\alpha$  are fitting constants. The variation of microstructural parameter  $\rho$  with  $\epsilon$  is given by,

$$\frac{d\rho}{d\epsilon} = M(K_1\sqrt{\rho} - K_2\rho) \quad (8)$$

where,  $K_1$  and  $K_2$  are coefficients of stage-II and stage III strain hardening.

Since dynamic recovery in metals during state III hardening is rate dependent, the coefficient  $K_2$  can be modelled [78],

$$K_2 = K_{20} \left( \frac{\dot{\epsilon}}{\dot{\epsilon}_0} \right)^{-\frac{1}{n}} \quad (9)$$

where,  $K_{20}$  and  $n$  are material constants and the exponent  $n$  is temperature dependent.

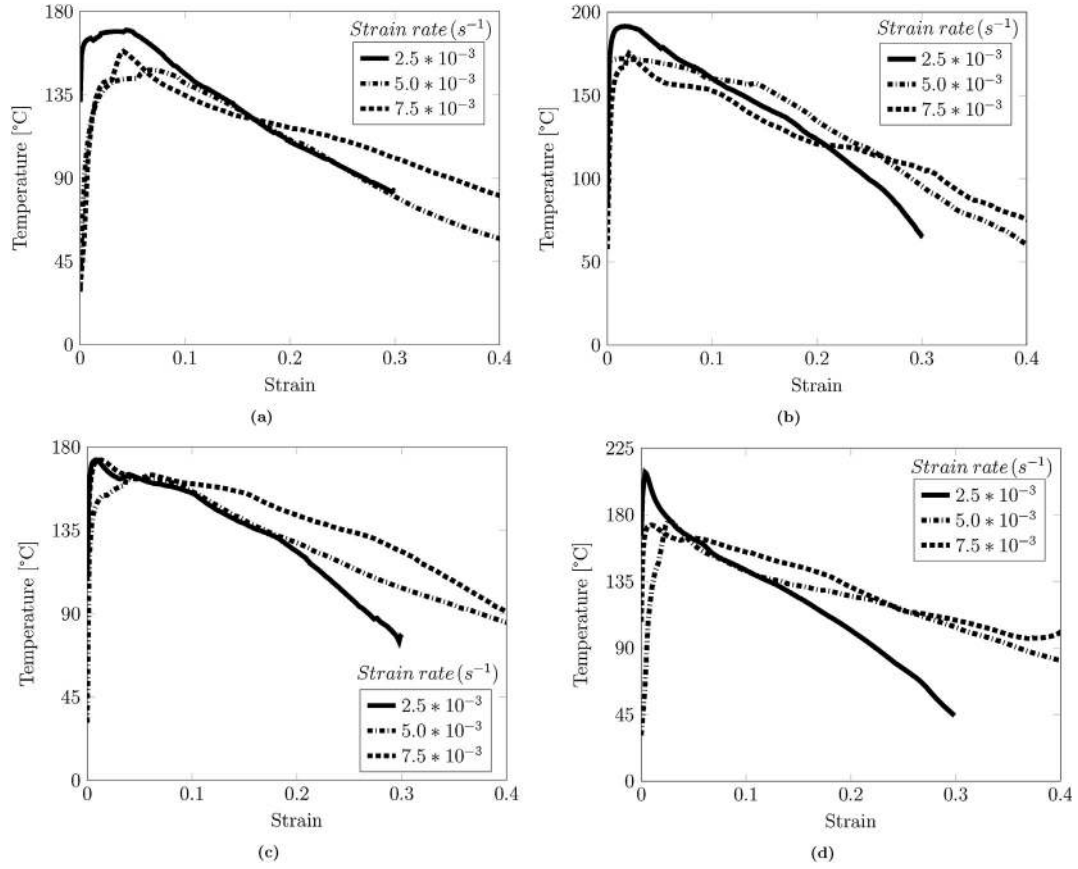


**Fig. 9 – Recorded temperatures at different strain rates during electric assisted compression tests are plotted with strain for different material conditions (a) STA, (b) CW, (c) NC and (d) NC + CW. Temperatures at strain rates of  $2.5 \times 10^{-3}$ ,  $5 \times 10^{-3}$  and  $7.5 \times 10^{-3} \text{ s}^{-1}$  are represented by solid, dashed dot and dashed lines respectively.**

The material constant  $\alpha$  in eq. (7) depends upon the fraction of obstacles, which usually decrease with increase in temperature due to thermal vibrations. Previous works [79,80] have successfully demonstrated the temperature and strain rate dependency of  $\alpha$ . In addition to  $\alpha$ , parameters such as  $m$  and  $\dot{\epsilon}_0$  in eq. (7) are also dependent on temperature and strain rate. Similarly, at low temperatures (typically  $T < 0.5T_m$ ),  $n$  in eq. (9) is temperature dependent. Following Conrad [38], the electroplastic effect influences the plastic strain rate and hence the above mentioned parameters should vary with 'J' under the application of electric current.

An explicit mathematical relation is not established for the above said parameters. Hariharan et al. [59,77] treated  $m$  and  $\dot{\epsilon}_0$  in eq. (7) as invariant and modelled rate effect in  $\alpha$  and  $n$  as

$$\alpha = \alpha_0 \beta_1 \left\{ \dot{\epsilon}^{\beta_2} T^{\beta_3} + \frac{\beta_4 J^{\beta_5}}{\beta_1} \right\} \quad (10)$$

$$n = \beta_6 \left\{ T^{\beta_7} + \frac{\beta_8 J^{\beta_9}}{\beta_6} \right\} \quad (11)$$

where,  $\alpha_0$ ,  $\beta_1$  to  $\beta_9$  are material constants. The constants  $\beta_4$ ,  $\beta_5$ ,  $\beta_8$  and  $\beta_9$  are used to describe the electroplastic effect for a current density 'J'.

Choosing the room temperature monotonic stress strain curve as reference, the parameters of dislocation density model is obtained by least square error minimization. The

variation of  $K_2$  and  $\alpha$  with temperature and strain rate is used to calibrate the material constants,  $\beta_1$ ,  $\beta_2$ ,  $\beta_3$ ,  $\beta_6$ ,  $\beta_7$  using eqns. (10) and (11). The temperature decoupled electroplastic data is used to estimate the remaining constants ( $\beta_4$ ,  $\beta_5$ ,  $\beta_8$ ,  $\beta_9$ ).

The material constants thus obtained for each microstructural condition is tabulated in Table 3. The resulting stress–strain curve from the model (Fig. 11a–d) is in good agreement with the experimental observations in each microstructural condition. It is to be emphasized that the above model accounted the electroplastic effect in thermal and athermal component of flow stress through  $n$  and  $\alpha$  respectively. As mentioned earlier, the above frame work is generic and can be applied to describe any electroplastic mechanism that assumes the influence of electric current on both the thermal and athermal flow stress components.

#### 4.3. Effect of strain on electroplastic effect

The electroplastic stress reduction ( $\Delta\sigma_{ep}$ ) generally increases with the strain in all the four microstructural conditions (Fig. 12a–d) due to its influence on dislocation behaviour.

A part of the dislocation density is mobile and contributes to thermal component of flow stress. The remaining forest dislocations that are athermal in nature increases the internal stress. It has been established [12,38] that the flow of electric current influences both the thermal ( $\propto J$ ) and athermal ( $\propto J^2$ )

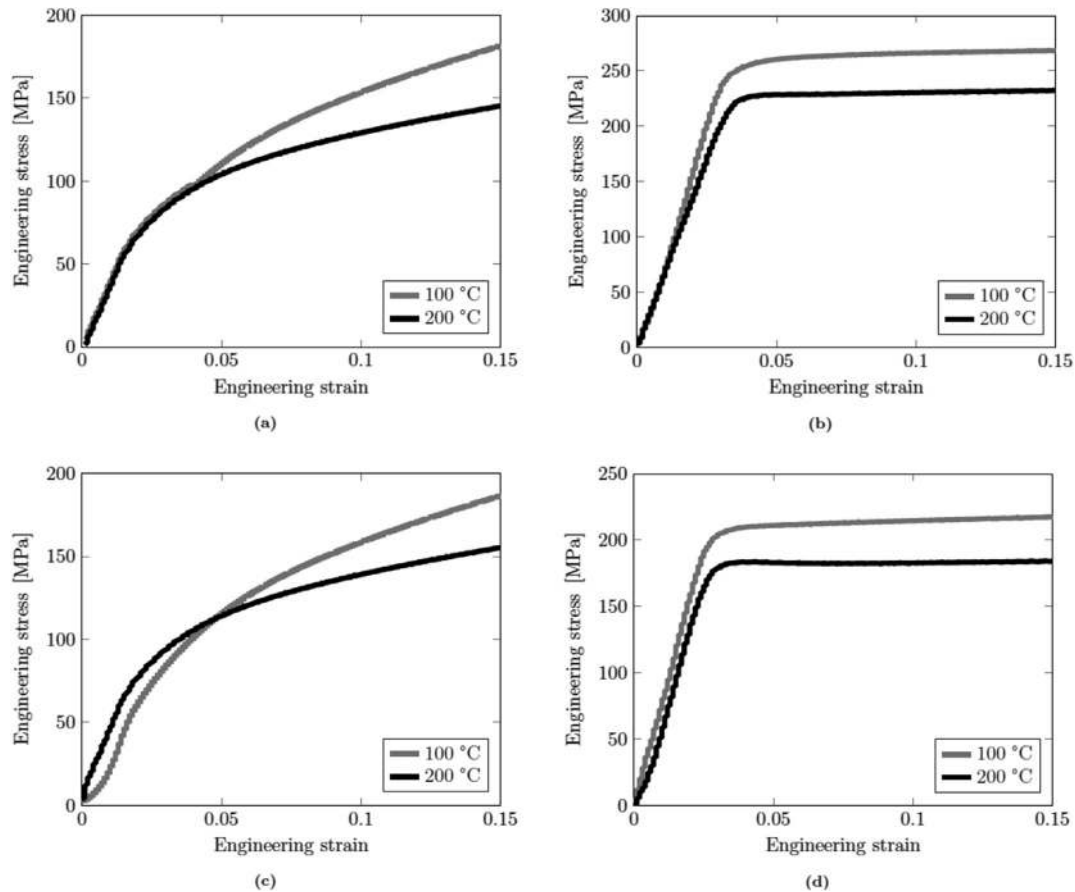


**Fig. 10 – Engineering stress–strain curve at isothermal condition. High temperature stress strain behaviour of four microstructural conditions (a) STA, (b) CW, (c) NC and (d) NC + CW is plotted. Stress strain curve at 100 °C and 200 °C is denoted by gray and black lines respectively.**

components [12]. The application of electric current complements the externally applied force to increase the velocity of dislocations thereby decreasing the thermal stress required to continue plastic deformation. As a consequence, the mobile dislocation density decreases by annihilation [81,82] and increases the average mean free path for dislocation motion. With strain the mobile dislocation density increases due to strain hardening leading to increased  $\Delta\sigma_{ep}$ . In fact, the variation of  $\Delta\sigma_{ep}$  with strain can be correlated directly with the strain hardening exponent of the material.

It has been shown [77] that the electroplastic effect in aged Al alloys is purely due to dislocation interaction where the inter-precipitate distance remain unaffected.  $\Delta\sigma_{ep}$  in CW is comparatively higher than that of STA, which is consistent with the results reported in the literature [83]. At  $\epsilon_p = 0$ ,  $\Delta\sigma_{ep}$  in CW is almost double the value of STA at  $2.5 \times 10^{-3} \text{ s}^{-1}$  strain rate. Severe cold working, as in the present case of CW, results in high density of forest dislocations. Both the thermal and athermal contribution of electroplasticity contributes to enhanced stress drop in CW. The cold rolling increases the misorientation of sub grains. Huang et al. [84] recently showed that the electron wind effect is pronounced in microstructure

with high misorientations, which can possibly explain the observed results.

In the case of NC samples, the dispersion of SiC particles retards the dislocation motion, which affects the annihilation due to electric current. The activation energy, upon which the thermal component of flow stress depends, is lesser in NC compared to STA [85]. Therefore the rate of change of  $\Delta\sigma_{ep}$  with strain in NC sample is lesser than that of STA samples. The influence of SiC is significant in cold worked state (NC + CW) as observed in Fig. 13a–c. It may be observed that, unlike STA and CW,  $\Delta\sigma_{ep}$  did not increase with dislocations in NC + CW samples. The stress drop in NC + CW with strain is similar or slightly less than that of NC Samples. Thus it may be inferred that the dispersion of nano-particles has a stronger influence on the suppression of electroplastic effect overcoming the contribution of dislocation density due to cold working.

It may be observed (Fig. 12c–d) that stress drop ( $\Delta\sigma_{ep}$ ) decreased slightly with strain while deforming NC and NC + CW samples at strain rate of  $7.5 \times 10^{-3} \text{ s}^{-1}$ . The reduction of electroplastic effect is however apparent and is due to the change in effective current density with strain. As mentioned

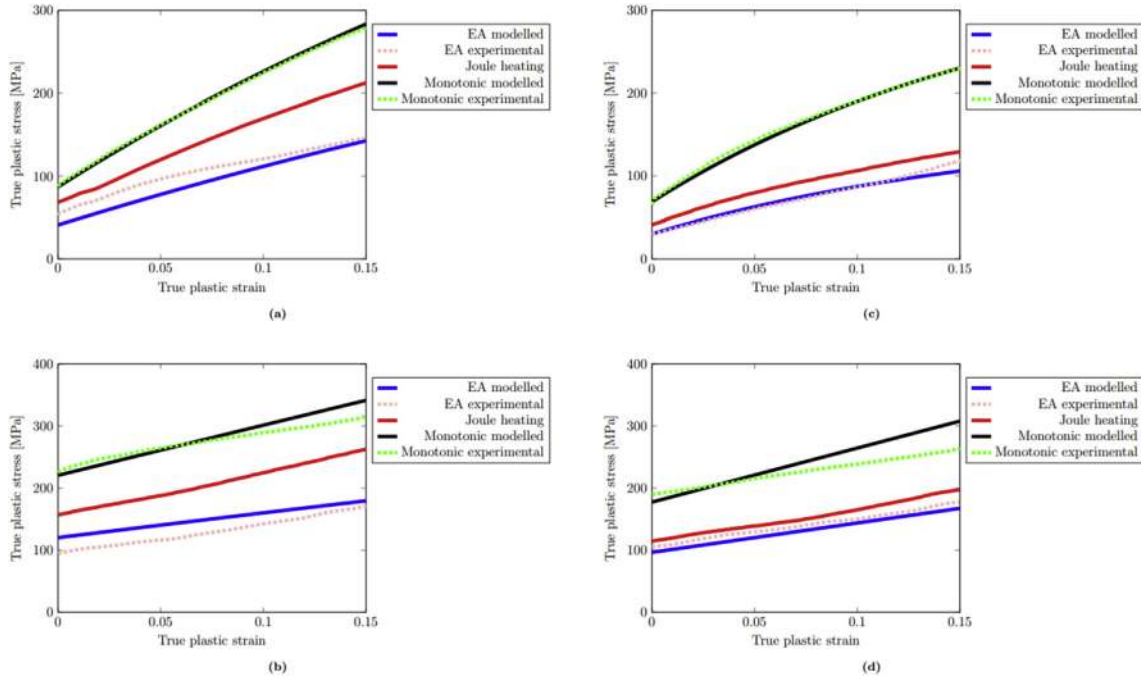


**Fig. 11 – True stress-true plastic strain response of monotonic, electric assisted and Joule heating effect for the material conditions (a)STA, (b)CW, (c)NC and (d)NC + CW. Experimental data is shown in dashed lines and the modelled curves are denoted by solid lines.**

earlier, the cross-sectional area of the specimen increases with strain during uniaxial compression. In the present work, the applied electric current is maintained constant and hence the current density decreases with strain. The change in instantaneous current density with the increment of strain is shown in Table 4. Experimentally electroplastic effect is observed only when the applied current density is above a critical threshold value, which is  $\approx 10 \text{ A mm}^{-2}$  for Al-alloys [39,86,87]. It is to be noted (Table 4) that the applied current density is above the threshold value even at maximum engineering strain of 0.15.

However, in all the other cases, stronger electroplastic effect leads to increase of  $\Delta\sigma_{ep}$  with strain albeit the continuous decrease of 'J'.

#### 4.4. Strain rate dependence

The rate dependent electroplastic effect is analysed by plotting  $\Delta\sigma_{ep}$  for different strain rate (Fig. 12a–d). It is observed that irrespective of the microstructure, for a given  $\epsilon_p$ ,  $\Delta\sigma_{ep}$  decreased with increasing strain rate. Similar trend of diminishing effect of electricity with increasing strain rate is reported in previous literature [39]. The importance of decoupling the thermal effect from the experimental data may be appreciated when analysing the strain rate effect on electroplasticity. At lower strain rate, the total electrical energy input (eq. (4)) is more due to longer time interval. As a result, the thermal softening due to Joule heating will be significant at lower strain rate. Considering plastic deformation as thermally activated flow, the strain rate can be represented as,  $\dot{\epsilon} = \dot{\epsilon}_0 \exp\left(\frac{-Q}{kT}\right)$  where,  $\dot{\epsilon}_0$  is the pre-exponential constant, Q,

k and T are activation energy, Boltzmann constant and temperature respectively. The temperature and rate effect can be coupled using the widely used Zener-Hollomon parameter,<sup>5</sup>  $Z = \dot{\epsilon} \exp\left(\frac{-Q}{RT}\right)$  with which the rate dependent flow stress is described as  $\sigma = f(Z)$ . The activation energy 'Q' in 'Z' can be additively superposed as,

$$(Q) = (Q)_T + (Q)_\dot{\epsilon} \tag{12}$$

where,  $(Q)_T$  and  $(Q)_\dot{\epsilon}$  represents the contribution from temperature and strain rate towards activation energy respectively.

Physically, the strain rate dependence on electroplastic effect is attributed to the modification of thermal component of flow stress that overcome the short-range obstacles [77]. The thermal component assists dislocation motion to overcome the activation barrier. In the absence of external current, the activation barrier can be overcome either by increasing the temperature or strain rate, both of which contributes to increase in dislocation energy to jump the activation barrier. Unlike temperature, the increase in strain rate is achieved mechanically and hence flow stress (and 'Z') increases with strain rate under isothermal condition. On contrary, increase in temperature decreases the mechanical stress (and 'Z') required. The experimental observations on the reduction of Young's modulus [88] and flow stress [89] due to application of external current is similar to the temperature effect. The

<sup>5</sup> Since the gas constant  $R = Nk$ , where, N is the Avogadro number, both R and k can be interchangeably used to describe the rate equation.

**Table 3 – Modelling parameters of STA, CW, NC and NC + CW microstructures in AA 6063 alloy.**

Notation	M	$\alpha_0$	G (MPa)	b (mm)	$K_1$	$K_{20}$
STA	3.5	0.055	27,000	$2.86 \times 10^{-7}$	10240	32
CW	3.5	0.078	27,000	$2.86 \times 10^{-7}$	20000	15
NC	3.5	0.067	27,000	$2.86 \times 10^{-7}$	18000	51
NC + CW	3.5	0.010	27,000	$2.86 \times 10^{-7}$	15500	25
Notation	1/m	$\dot{\epsilon}_0$ ( $s^{-1}$ )	$\rho_0$ ( $mm^{-2}$ )	$\beta_1$	$\beta_2$	$\beta_3$
STA	0.82	$1.5 \times 10^{-7}$	$7.5 \times 10^5$	1.0	0.05	-0.76
CW	0.85	$1.5 \times 10^{-7}$	$8.5 \times 10^7$	1.0	0.33	-0.89
NC	1.05	$1.5 \times 10^{-7}$	$1.25 \times 10^6$	1.0	0.96	-0.54
NC + CW	1.07	$1.5 \times 10^{-7}$	$3.0 \times 10^7$	1.0	0.22	-1
Notation	$\beta_4$	$\beta_5$	$\beta_6$	$\beta_7$	$\beta_8$	$\beta_9$
STA	-0.0052	0.01	0.27	0.45	0.35	0.44
CW	-0.0005	0.06	0.27	0.35	0.43	0.56
NC	-0.0002	0.125	0.19	0.52	0.16	0.12
NC + CW	-0.0005	0.02	0.31	0.28	0.05	0.15

electroplastic effect can be modelled [59] by accounting its contribution to activation energy as

$$(Q) = (Q)_T + (Q)_\dot{\epsilon} + (Q)_J \quad (13)$$

where, J represent the current density. From eq. (12), it may be inferred that at high strain rates, flow stress reduction due to temperature change ( $\Delta T$ ) is relatively less. Extending the

above argument, under isothermal condition  $\Delta\sigma_{ep}$  should decrease with increase in strain rate, as shown in Fig. 12a–d.

Liu et al. [90] made similar inference that  $\Delta\sigma_{ep}$  is inversely proportional to 'Z'. Following the above discussed trend,  $\Delta\sigma_{ep}$  is lesser at higher  $\dot{\epsilon}$  in all the microstructure (Fig. 13a–c). Although  $\Delta\sigma_{ep}$  in cold worked sample is higher, it is less sensitive to  $\dot{\epsilon}$  when compared to solution treated samples.

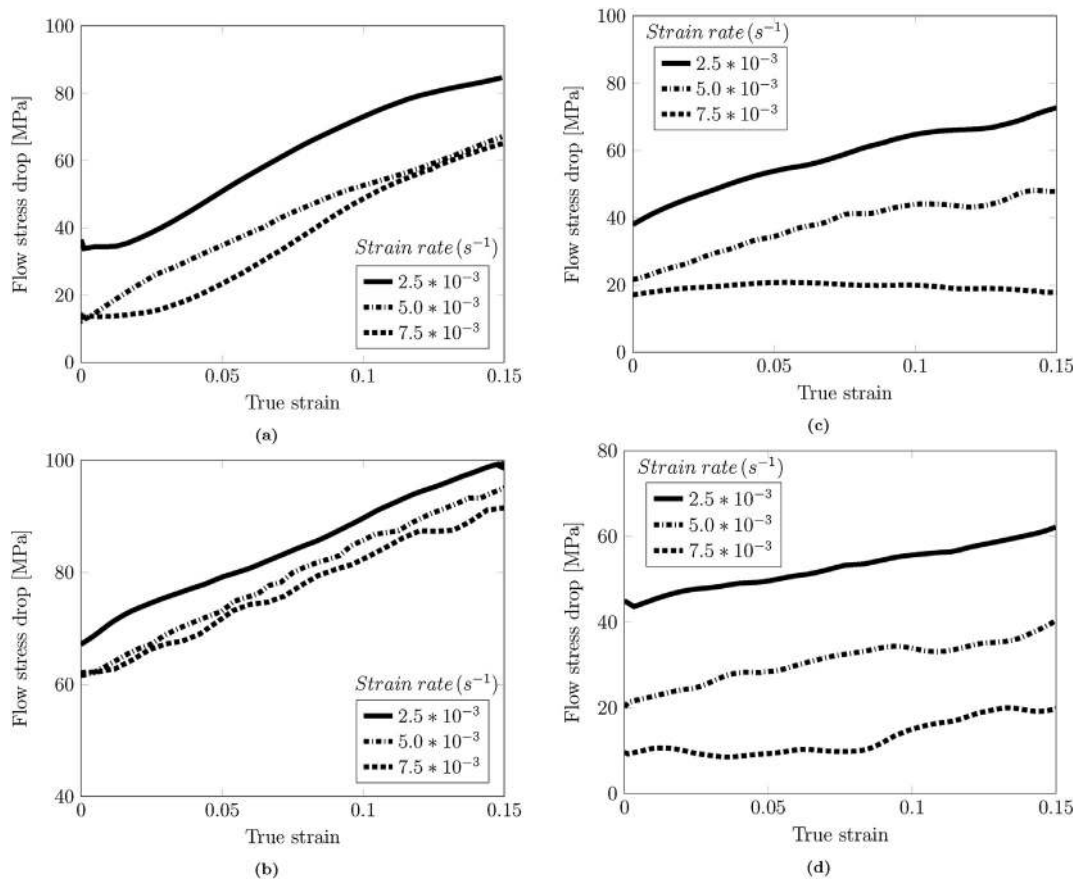


**Fig. 12 – Stress reductions due to electroplasticity at different strain rates for microstructural conditions of (a) STA, (b) CW, (c) NC and (d) NC + CW. Stress reductions calculated at strain rates of  $2.5 \times 10^{-3}$ ,  $5 \times 10^{-3}$  and  $7.5 \times 10^{-3} s^{-1}$  are represented by solid, dashed dot and dashed lines respectively.**

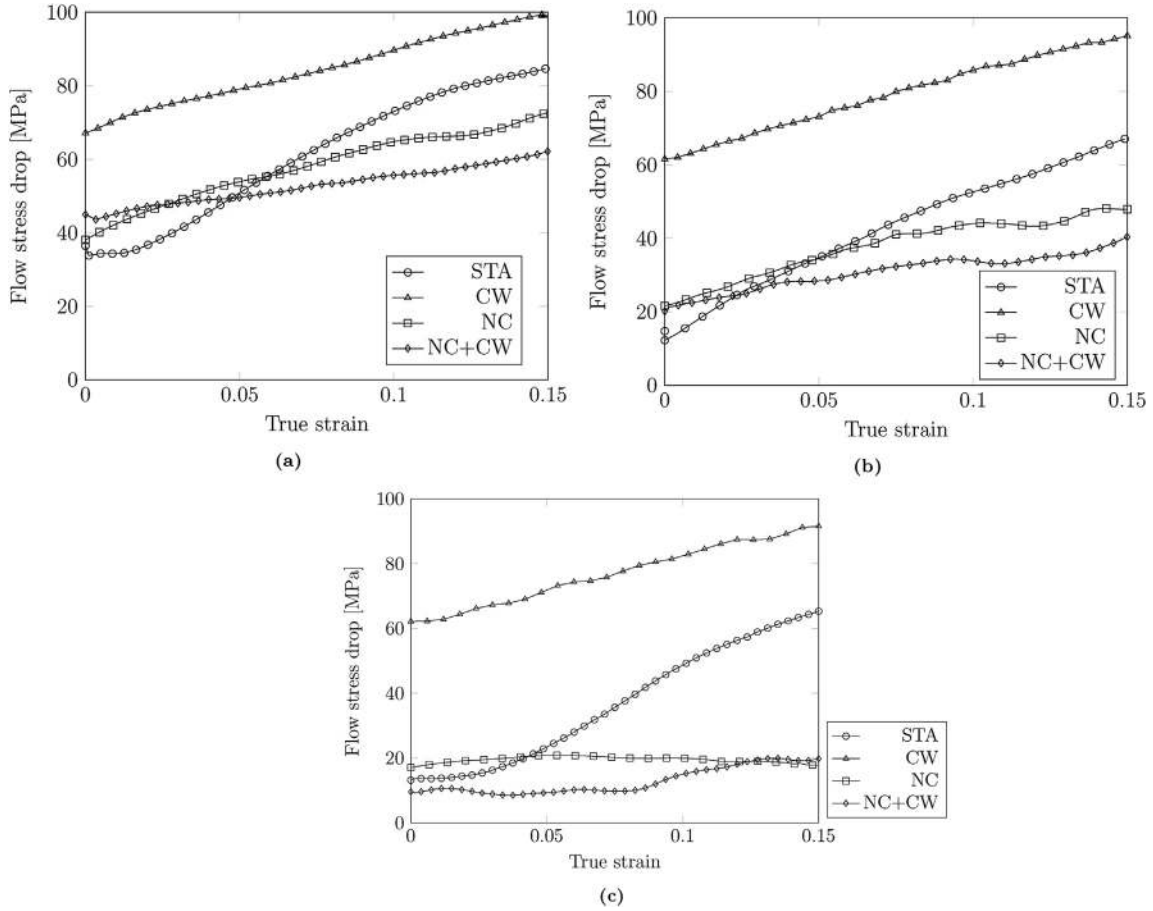


**Fig. 13 – Stress drop due to electroplastic effect in four microstructural conditions of STA, CW, NC and NC + CW at strain rates of (a)  $2.5 \times 10^{-3}$ , (b)  $5 \times 10^{-3}$  and (c)  $7.5 \times 10^{-3} \text{ s}^{-1}$ .**

However, in the case of NC samples, the cold working did not affect the sensitivity with strain rate.

**4.5. X-ray diffraction analysis**

The deformed samples (with and without current) are subjected to X-ray diffraction analysis and the resulting peaks obtained are fit using Pseudo-Voigt function. The Voigt function is a convolution of Gaussian and Lorentzian functions. It is often [91–93] used as a peak profile where neither a pure Gaussian or Lorentzian function appropriately describe a peak for the data. Instead of convoluting those two functions, the Pseudo-Voigt function is defined as the sum of a Gaussian  $G_n$  and a Lorentzian components  $L_n$ , weighted by a parameter ( $\mu_n$ ), which shifts the profile more towards pure Gaussian or pure Lorentzian, as applicable. The minimization function in the fitting program [94,95] is given as:

$$\sum \left( I - \left\{ I_0 + \sum_n A_n [\mu_n L_n + (1 - \mu_n) G_n] \right\} \right) \quad (14)$$

Lorentzian function  $L_n$  and Gaussian function  $G_n$  are given in eq. 15

$$L_n = \frac{1}{1 + \left( \frac{x_i - x_c^n}{w^n} \right)^2} \quad (15)$$

$$G_n = \exp \left[ -0.5 \left( \frac{x_i - x_c^n}{w^n} \right)^2 \right]$$

where,  $I_0$  is the background intensity,  $I$  is the recorded intensity of  $x_i$ <sup>th</sup> peak,  $\mu$  is the Lorentz fraction,  $A_n$  is the amplitude of  $n$ th peak,  $x_c$  is the coordinate position of centre of the peak and  $w^n$  is the width of  $n$ th peak.  $L_n$  represents the contribution of dislocation density in the peak and  $G_n$  represents internal stress profile.

Lorentzian contribution is used to compare the dislocation density with and without assistance of current. The results for all four microstructural conditions are tabulated in Table 5. As evident from the results, Lorentzian function increases due to the presence of higher dislocations in cold worked state (CW and NC + CW conditions). In case of EA tests, Lorentzian function has decreased, indicating the reduction of dislocation density due to the annihilation of dislocations in presence of electric current.

**Table 4 – Change in instantaneous current density with increasing strain.**

Engg. strain	Instantaneous diameter (mm)	Instantaneous area (mm <sup>2</sup> )	Instantaneous current density (A mm <sup>-2</sup> )
0	2	3.14	19.45
0.1	2.11	3.49	17.51
0.15	2.17	3.70	16.52

Lorentzian contributions representing dislocation density for different microstructures with and without assistance of current are compared in Fig. 14.

The reduction in dislocation density evident from Fig. 14 confirms the dislocation annihilation under the influence of moving electrons as discussed in the earlier sections. Although, the reduction in Lorentzian contribution is consistent in all the four microstructural condition, the magnitude of reduction in case of NC is less compared to other conditions. As discussed in section 4.1, this indicates that the role of nano-particles in pinning the dislocations and thus reducing the dislocation annihilation. In NC + CW, the effect of cold working is apparent with reduction in Lorentzian contribution being higher than the NC condition.

#### 4.6. Discussion on contributing mechanisms

Among the various mechanisms [55] proposed, Joule heating, electron wind effect and depinning of dislocations due to current induced magnetic field are widely used [53]. Based on the literature (section 1) and results after decoupling the thermal effects in section 4.1, it is clear that the observed electroplastic effect cannot be explained completely by Joule heating. Localized resistive heating or heterogeneous Joule heating [74,96] is often used to explain electroplasticity in metals. The theory can successfully explain the observation of localized grain boundary melting and increased electroplastic effect in fine grained materials [33]. Accordingly, the presence of grain boundaries, dislocation pile up and other obstacles can enhance the electroplastic effect due to heterogeneous electrical resistance. In the present work, the STA and CW samples showed significant electroplastic effect when compared to NC and NC + CW. The heterogeneity of electrical resistance however increases with the nano-particles. Therefore it is inferred that heterogeneous Joule heating is not the governing mechanism for the observed electroplastic effect in the investigated alloys.

**Table 5 – Lorentzian function of deformed samples (with and without assistance of electrical current) in STA, CW, NC and NC + CW microstructural condition.**

Microstructural condition	Ln contribution	Ln contribution
	(With current)	(Without current)
STA	0.079 ± 0.012	0.091 ± 0.011
CW	0.088 ± 0.012	0.102 ± 0.015
NC	0.101 ± 0.018	0.109 ± 0.010
NC + CW	0.102 ± 0.018	0.117 ± 0.020

Electron wind effect is the earliest theory proposed to explain the electroplastic effect. According to the theory, the momentum transfer between moving electrons and dislocations contributes to increment in thermal stress, and is proportional to the applied current density ( $\sigma_{ew}^* \propto J$ ); where the subscript 'ew' refers to electron wind.  $\sigma_{ew}^*$  augments the thermal stress in the expression for activation energy as

$$\Delta G = \Delta G_0 - (\sigma^* + \sigma_{ew}^*)V^* \quad (16)$$

where,  $\Delta G$  is the activation energy assuming small changes in the thermal stress,  $\sigma^*$  and  $V^*$  are thermal component of flow stress and activation volume respectively.

Since  $\dot{\epsilon}$  for thermally activated deformation is given as,  $\dot{\epsilon} = \dot{\epsilon}_0 \exp\left(\frac{-Q}{kT}\right)$ , change in  $\Delta G$  due to  $\sigma_{ew}^*$  in eq. (16) leads to local increment in strain rate. Conrad [38] phenomenologically modelled the change in strain rate as

$$\frac{(\dot{\epsilon})_J}{(\dot{\epsilon})_{J=0}} = \left(\frac{J}{J_c}\right)^\lambda \quad (17)$$

where,  $J_c$  is the threshold current density and  $\lambda$  a fitting constant.

If other factors in  $\dot{\epsilon}$  remain unaffected by  $J$ ,  $\Delta\sigma_{ep}$  would be equal to  $\sigma_{ew}^*$ . With increase in strain,  $V^*$  decreases due to strain hardening. This results in reduction of  $\Delta\sigma_{ep}$  (from eq. (16)), contradictory to that reported in literature [28,59,71] and the results presented in section 4.3. It is shown [46] that factors including  $\dot{\epsilon}_0$ ,  $V^*$  and  $\Delta G_0$  has a strong influence on the electroplastic deformation that can explain the observed results. The mobile dislocation density increases with strain [97]. As pointed out in [59], the stress drop due to annihilation is proportional to the mobile dislocation density and contributes to increased  $\Delta\sigma_{ep}$  with strain. The higher  $\Delta\sigma_{ep}$  in CW sample when compared to STA can be explained following similar argument that the increased dislocation density in CW samples increases the mobility of dislocations and HAGs. The SiC particles in NC and NC + CW act as barriers against dislocation annihilation and hence the stress drop due to electroplasticity is less than STA and CW respectively. Unlike CW, NC + CW does not show significant increase in  $\Delta\sigma_{ep}$  when compared to NC samples. In fact, the electroplastic effect in NC + CW at higher strain is often less than NC. It is presumed that the rolling of NC samples deforms and redistributes the SiC particles, which reduces the effectiveness of the obstacles. This is corroborated by the fact that the change in Lorentzian component (Fig. 14) with and without current

**Table 6 – Change in stress drop due to electroplasticity ( $\Delta\sigma_{ep}$ ) and strain hardening exponent ( $n$ ) as a function of strain and strain rate in STA, CW, NC and NC + CW microstructural condition.**

Microstructural condition	Strain rate ( $s^{-1}$ )					
	$2.5 * 10^{-3}$		$5.0 * 10^{-3}$		$7.5 * 10^{-3}$	
	$\Delta\sigma_{ep}$	$n$	$\Delta\sigma_{ep}$	$n$	$\Delta\sigma_{ep}$	$n$
STA	48.2	321.33	52.3	348.67	52.1	347.33
CW	31.4	209.33	33.5	223.33	29.4	196.00
NC	34.7	231.33	26.2	174.67	-0.73	-4.87
NC + CW	17.1	114.00	20.2	134.67	10.2	68.00

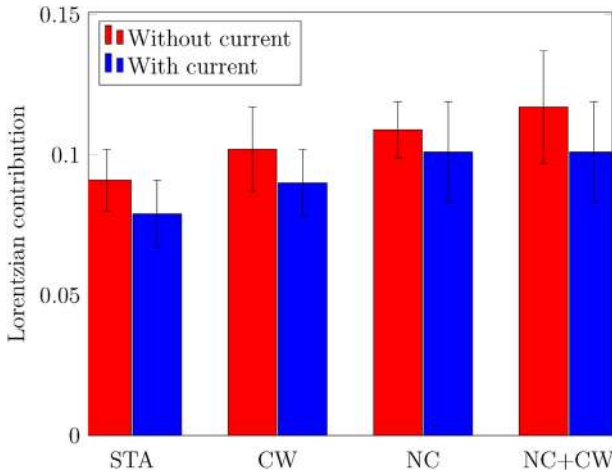


**Fig. 14 – Comparison of Lorentzian contribution of deformed samples with and without assistance of current in STA, CW, NC and NC + CW microstructural conditions. Error in the calculation of Lorentzian contribution is denoted by the respective error bars in the figure.**

in NC sample is less than that of NC + CW. The rate of change of  $\Delta\sigma_{ep}$  with strain depends upon the strain hardening rate as it correlates with the rate at which mobile dislocations are generated. In the present work, the rate of change of  $\Delta\sigma_{ep}$  with strain at a strain rate of  $2.5 * 10^{-3} s^{-1}$  is in the order of  $STA > NC > CW > NC + CW$  (Table 6).

The above trend is not observed at higher strain rates; rate of change of  $\Delta\sigma_{ep}$  with strain in NC decreases rapidly with increase in strain rate ( $5 * 10^{-3} s^{-1}$  and  $7.5 * 10^{-3} s^{-1}$ ). Therefore, mechanisms other than electron wind control the electroplastic deformation.

Molotskii and Fleurov [52] proposed that the electroplastic deformation is due to the current induced magnetic field causing depinning of dislocations from the obstacles. One of the main objections for the electron wind theory is the overestimation of the ratio  $\Delta\sigma_{ew}/J$  when compared to experiments. However as clarified by Conrad [38], the magnetic effect could be one of the contributing factors of the strong dependence of 'J' on the pre-exponential  $\epsilon_{90}$ . Recently, Andre et al. [98] using nano-indentation and Lahiri et al. [53] using crystal

plasticity simulations showed that the depinning of dislocation at obstacles is the main contributor than the thermal effects. The magnetic effect of depinning successfully explains the weak polarity dependence of electroplasticity [52]. Since the forest dislocations are paramagnetic [99] in nature, the increased electroplastic effect with strain observed in all the microstructure can be successfully explained using the theory. The high  $\Delta\sigma_{ep}$  in CW compared to STA is also in agreement with the theory. The electroplastic effect in NC is always less than that of STA. Although the presence of SiC particles increases the obstacles of dislocations, unlike forest dislocation, SiC particles are not paramagnetic [100]. Therefore, the SiC particles does not facilitate depinning, but rather arrests the depinned dislocations by magnetic field effect on forest dislocations. The above argument can be extended to explain the relatively lower rate of change of  $\Delta\sigma_{ep}$  in NC against STA as well. The role of NC in NC + CW is complex, considering the possible changes induced by cold rolling. The difference between NC and NC + CW is rather less than that of STA and CW, which suggests the strong role of SiC particles in both NC and NC + CW samples.

The electroplastic behaviour of all the samples investigated can be qualitatively explained by combining electron wind effect for thermal component of flow stress and magnetic depinning for the pre-exponential factor. Although the exact role and mode of interaction of electron flow with dislocations and other obstacles warrant further studies [55], the present work offers sufficient inputs for phenomenological modelling of electroplastic effect in the investigated materials with different microstructure.

## 5. Conclusions

Compressive deformation with and without the application of electric current is performed on AA 6063 samples with different microstructures. The application of electric current is found to produce significant changes in the flow behaviour of the samples in each microstructural condition. The Joule heating effect is decoupled from the experimental results by interpolating the flow stress obtained from isothermal compression tests at different temperature. The observations can be summarized as follows:

1. Stress drop is observed in all the cases when the deformation took place in the presence of electric current. It is also observed that the drop in flow stress due to electric assisted deformation is strongly related to the initial microstructure of the material. The presence of SiC in nano composites suppressed the electron–dislocation interaction in both solutionized and cryorolled condition.
2. Decoupling the Joule heating effect during the application of constant amplitude current is complex due to the temperature dependence of electrical resistance and thermal conductivity. Direct measurements of temperature history was used to decouple the electrical effect. The results (flow stress drop) thus obtained is a function of initial microstructure and strain rate and can serve as input for constitutive modelling.
3. The flow stress reduction exhibited a strong dependence on strain rate. The inverse relation of the flow stress drop with the Zener-Hollomon parameter confirms the role of thermal component in the mechanism.
4. The reduction of Lorentzian component during X-ray diffraction towards the peak confirms the annihilation of dislocations during electric assisted deformation. The role of SiC on reduced electroplastic effect is further evidenced from the relatively smaller reduction of Lorentzian component in both NC and NC + CW compared to STA and CW. The observations support the role of paramagnetic obstacles in depinning the dislocations for enhanced plastic deformation. The ferromagnetic obstacles such as SiC in nano composites exhibits a passive role.
5. Based on the trend of variation of electroplastic effect, it is concluded that neither heterogeneous Joule heating nor classical electron wind effect can independently explain the observations. Therefore, it is concluded that magnetic depinning of dislocations could be the rate controlling mechanism of the investigated aluminium alloys and nano composites, supported by other mechanisms like electron wind effect and heterogeneous heating.

---

### Declaration of competing interest

The authors declare that they have no known competing financial interests or personal relationships that could have appeared to influence the work reported in this paper.

---

### Acknowledgements

Authors would like to acknowledge the financial support from Science and Engineering Research Board (Project reference: CRG/2019/003539), Department of Science and Technology (DST) India. Authors also would like to thank Mr. C. Venkatesh who developed the compression test fixture as a part of his Master's thesis for electric assisted experiments.

### REFERENCES

---

- [1] Ross CD, Kronenberger TJ, Roth JT. Effect of DC on the formability of Ti–6Al–4V. *J Eng Mater Technol* 2009;131(3):031004.
- [2] Prasad K, Krishnaswamy H, Jain J. Leveraging transient mechanical effects during stress relaxation for ductility improvement in aluminium AA 8011 alloy. *J Mater Process Technol* 2018;255:1–7.
- [3] Kravchenko VY. Effect of directed electron beam on moving dislocations. *Sov Phys JETP* 1967;24(6):1135–42.
- [4] Pustovalov V, Startsev V, Fomenko V. Plastic deformation of lead in the normal and superconducting states. *Phys Status Solidi (B)* 1970;37(1):413–23.
- [5] Kravchenko V. Influence of electrons in delaying dislocation in metals. *JETP (USSR)* 1966;51:1676.
- [6] Klimov K, Novikov I. The “electroplastic effect”. *Strength Mater* 1984;16(2):270–6.
- [7] Roshchupkin A, Miloshenko V, Kalinin V. The electron retardation of dislocations in metals. *Fiz Tverd Tela* 1979;21(3):909–10.
- [8] Troitskii O, Likhman V. The anisotropy of the action of electron and  $\gamma$ -radiation on the deformation of zinc single crystals in the brittle state. *SPhD* 1963;8:91.
- [9] Timsit R. Remarks on recent experimental observations of the electroplastic effect. *Scripta Metall* 1981;15(4):461–4.
- [10] Goldman P, Motowidlo L, Galligan J. The absence of an electroplastic effect in lead at 4.2 k. *Scripta Metall* 1981;15(4):353–6.
- [11] Okazaki K, Kagawa M, Conrad H. A study of the electroplastic effect in metals. *Scripta Metall* 1978;12(11):1063–8.
- [12] Sprecher A, Mannan S, Conrad H. Overview no. 49: On the mechanisms for the electroplastic effect in metals. *Acta Metall* 1986;34(7):1145–62.
- [13] Okazaki K, Kagawa M, Conrad H. An evaluation of the contributions of skin, pinch and heating effects to the electroplastic effect in titanium. *Mater Sci Eng* 1980;45(2):109–16.
- [14] Andrawes JS, Kronenberger TJ, Perkins TA, T RJ, Warley RL. Effects of DC current on the mechanical behavior of AlMg1SiCu. *Mater Manuf Process* 2007;22(1):91–101.
- [15] Roth JT, Loker I, Mauck D, Warner M, Golovashchenko SF, Krause A. Enhanced formability of 5754 aluminium sheet metal using electric pulsing. In: *Transactions of the North American manufacturing research institution of SME. Society of Manufacturing Engineers*; 2008. p. 405–12.
- [16] Salandro WA, Khalifa A, Roth JT. Tensile formability enhancement of magnesium AZ31B-0 alloy using electrical pulsing. In: *37th annual North American Manufacturing Research Conference, NAMRC, vol. 37*; 2009. p. 387–94.
- [17] Gennari C, Pezzato L, Simonetto E, Gobbo R, Forzan M, Calliari I. Investigation of electroplastic effect on four grades of duplex stainless steels. *Materials* 2019;12(12):1911.
- [18] Simonetto E, Bruschi S, Ghiotti A. Electroplastic effect on AA1050 plastic flow behavior in H24 tempered and fully annealed conditions. *Procedia Manuf* 2019;34:83–9.
- [19] Sánchez Egea A, Peiró JJ, Signorelli JW, González Rojas H, Celentano DJ. On the microstructure effects when using electropulsing versus furnace treatments while drawing inox 308L. *J Mater Res Technol* 2019;8(2):2269–79.
- [20] Lee J, Bong HJ, Lee Y-S, Kim D, Lee M-G. Pulsed electric current V-Bending springback of AZ31B magnesium alloy sheets. *Metall Mater Trans A* 2019;50(6):2720–31.
- [21] Green CR, McNeal TA, Roth JT. Springback elimination for Al6111 alloys using electrically assisted manufacturing

- (EAM). In: 37th Annual North American Manufacturing Research Conference, NAMRC, vol. 37; 2009. p. 403–10.
- [22] Pleta AD, Krugh MC, Nihare C, Roth JT. An investigation of anisotropic behavior on 5083 aluminum alloy using electric current. In: International Manufacturing Science and Engineering Conference collocated with the 41st North American Manufacturing Research Conference. ASME; 2013. p. V001T01A018.
- [23] Liu R, Wang W, Chen H, Wan S, Zhang Y, Yao R. Comparative study of recrystallization behaviour and nanoindentation properties of micro-/nano-bimodal size B4C particle-reinforced aluminium matrix composites under T6 and electropulsing treatment. *J Alloys Compd* 2019;788:1056–65.
- [24] Yiu P, Jang J, Chang S, Chen Y, Chu J, Hsueh C. Plasticity enhancement of Zr-based bulk metallic glasses by direct current electropulsing. *J Alloys Compd* 2012;525:68–72.
- [25] Yiu P, Chen Y, Chu J, Chang S, Bei H, Jang J, et al. Rapid relaxation and embrittlement of Zr-based bulk metallic glasses by electropulsing. *Intermetallics* 2013;34:43–8.
- [26] Huang Y, Fan H, Guan S, Ning Z, Cao F, Daisenber D, et al. Fine tuning the microstructure and mechanical properties of a Zr-based bulk metallic glass using electropulsing treatment. *J Alloys Compd* 2019;789:704–11.
- [27] Ho PS, Kwok T. Electromigration in metals. *Rep Prog Phys* 1989;52(3):301–48.
- [28] Siopis MS, Kinsey BL. Experimental investigation of grain and specimen size effects during electrical-assisted forming. *J Manuf Sci Eng* 2010;132(2):021004.
- [29] Wang X, Xu J, Shan D, Guo B, Cao J. Effects of specimen and grain size on electrically-induced softening behavior in uniaxial microtension of AZ31 magnesium alloy: experiment and modeling. *Mater Des* 2017;127:134–43.
- [30] Zhang H, Zhang C, Han B, Qiu J, Li H, Qin S, et al. Evolution of grain boundary character distributions in a cold-deformed Nickel-based superalloy during electropulsing treatment. *J Mater Res Technol* 2020;9(3):5723–34.
- [31] Kim M-J, Lee K, Oh KH, Choi I-S, Yu H-H, Hong S-T, et al. Electric current-induced annealing during uniaxial tension of aluminum alloy. *Scripta Mater* 2014;75:58–61.
- [32] Zhang X, Li H, Zhan M, Zheng Z, Gao J, Shao G. Electron force-induced dislocations annihilation and regeneration of a superalloy through electrical in-situ transmission electron microscopy observations. *J Mater Sci Technol* 2020;36:79–83.
- [33] Fan R, Magargee J, Hu P, Cao J. Influence of grain size and grain boundaries on the thermal and mechanical behavior of 70/30 brass under electrically-assisted deformation. *Mater Sci Eng: A* 2013;574:218–25.
- [34] Zeng Z, He J, Xiang Z, Sun Q, Wu Y, Wang S. Embrittlement of 316L stainless steel in electropulsing treatment. *J Mater Res Technol* 2020;9(5):10669–78.
- [35] Zhang W, Sui M, Hu K, Li D, Guo X, He G, et al. Formation of nanophases in a Cu–Zn alloy under high current density electropulsing. *J Mater Res* 2000;15(10):2065–8.
- [36] Zhu Y, To S, Liu X, Hu G. Effect of static electropulsing on microstructure and elongation of a Zn–Al alloy (ZA22). *Metall Mater Trans A* 2011;42(7):1933–40.
- [37] Dzialo C, Siopis M, Kinsey BL, Weinmann K. Effect of current density and zinc content during electrical-assisted forming of copper alloys. *CIRP Annals* 2010;59(1):299–302.
- [38] Conrad H. Electroplasticity in metals and ceramics. *Mater Sci Eng: A* 2000;287(2):276–87.
- [39] Perkins TA, Kronenberger TJ, Roth JT. Metallic forging using electrical flow as an alternative to warm/hot working. *J Manuf Sci Eng* 2006;129(1):84–94.
- [40] Kronenberger TJ, Johnson DH, Roth JT. Coupled multifield finite element analysis model of upsetting under an applied direct current. *J Manuf Sci Eng* 2009;131(3):031003.
- [41] Jones JJ, Mears L, Roth JT. Electrically-assisted forming of Magnesium AZ31: Effect of current magnitude and deformation rate on forgeability. *J Manuf Sci Eng* 2012;134(3):034504.
- [42] Hariharan K, Lee M-G, Kim M-J, Han HN, Kim D, Choi S. Decoupling thermal and electrical effect in an electrically assisted uniaxial tensile test using finite element analysis. *Metall Mater Trans A* 2015;46(7):3043–51.
- [43] Lee J, Kim S-J, Lee M-G, Song JH, Choi S, Han HN, et al. Experimental and numerical study on the deformation mechanism in AZ31B Mg alloy sheets under pulsed electric-assisted tensile and compressive tests. *Metall Mater Trans A* 2016;47(6):2783–94.
- [44] Troitskii O. Electromechanical effect in metals. *ZhETF Pisma Redaktsiiu* 1969;10:18.
- [45] Li D, Yu E, Liu Z. Microscopic mechanism and numerical calculation of electroplastic effect on metal's flow stress. *Mater Sci Eng: A* 2013;580:410–3.
- [46] Conrad H, Sprecher A, Cao W, Lu X. Electroplasticity—the effect of electricity on the mechanical properties of metals. *JOM (J Occup Med)* 1990;42(9):28–33.
- [47] Conrad H. Thermally activated plastic flow of metals and ceramics with an electric field or current. *Mater Sci Eng: A* 2002;322(1–2):100–7.
- [48] Cao W, Sprecher A, Conrad H. Measurement of the electroplastic effect in Nb. *J Phys E Sci Instrum* 1989;22(12):1026.
- [49] Baryshev G, Golovin YI, Kiperman V, Sletkov AA. Structural changes in the metal in the vicinity of holes and inclusions under current pulses. *Fiz Khim Obrab Mater* 1980;(4):12–5.
- [50] Beklemishev N, Koryagin N, Shapiro G. About plastic deformation of some conducting materials in an impulsive electromagnetic field, *Izvestiia Akademii nauk SSSR. Metall* 1985;(1):159–61 (1985).
- [51] Kukudzhanov V, Kolomiets-Romanenko A. A model of thermoelectroplasticity of variations in the mechanical properties of metals based on defect structure reorganization under the action of pulse electric current. *Mech Solid* 2011;46(6):814–27.
- [52] Molotskii M, Fleurov V. Magnetic effects in electroplasticity of metals. *Phys Rev B* 1995;52(22):15829.
- [53] Lahiri A, Shanthraj P, Roters F. Understanding the mechanisms of electroplasticity from a crystal plasticity perspective. *Model Simulat Mater Sci Eng* 2019;27(8):085006.
- [54] Dubinko V, Klepikov V. Kinetic mechanism of the electroplastic effect in metals. *Bull Russ Acad Sci Phys* 2008;72(9):1188–9.
- [55] Dimitrov NK, Liu Y, Horstemeyer M. Electroplasticity: a review of mechanisms in electro-mechanical coupling of ductile metals. *Mech Adv Mater Struct* 2020;1:1–12.
- [56] Roh J-H, Seo J-J, Hong S-T, Kim M-J, Han HN, Roth JT. The mechanical behavior of 5052-H32 aluminum alloys under a pulsed electric current. *Int J Plast* 2014;58:84–99.
- [57] Kim M-J, Jeong H-J, Park J-W, Hong S-T, Han HN. Modified Johnson-Cook model incorporated with electroplasticity for uniaxial tension under a pulsed electric current. *Met Mater Int* 2018;24(1):42–50.
- [58] Wang X, Xu J, Shan D, Guo B, Cao J. Modeling of thermal and mechanical behavior of a magnesium alloy AZ31 during electrically-assisted micro-tension. *Int J Plast* 2016;85:230–57.
- [59] Krishnaswamy H, Kim MJ, Hong S-T, Kim D, Song J-H, Lee M-G, et al. Electroplastic behaviour in an aluminium alloy and dislocation density based modelling. *Mater Des* 2017;124:131–42.

- [60] Dimitrov N, Liu Y, Horstemeyer M. An electroplastic internal state variable (ISV) model for nonferromagnetic ductile metals. *Mech Adv Mater Struct* 2020;1:1–12.
- [61] Aurrekoetxea M, López de Lacalle LN, Llanos I. Machining stresses and initial geometry on bulk residual stresses characterization by on-machine layer removal. *Materials* 2020;13(6):1445.
- [62] Fayomi OSI, Abdulwahab M, Popoola API, Asuke F. Corrosion resistance of AA6063-Type Al-Mg-Si alloy by silicon carbide in sodium chloride solution for marine application. *J Mar Sci Appl* 2015;14(4):459–62.
- [63] Pratikno H. Aging treatment to increase the erosion-corrosion resistance of AA6063 alloys for marine application. *Procedia Earth Planet Sci* 2015;14:41–6.
- [64] Krahmer DM, Polvorosa R, De Lacalle LL, Alonso-Pinillos U, Abate G, Riu F. Alternatives for specimen manufacturing in tensile testing of steel plates. *Exp Tech* 2016;40(6):1555–65.
- [65] Jung J, Ju Y, Morita Y, Toku Y, Uematsu Y. Delaying effect of high-density electric current on fatigue crack growth in AA 6061-T6 aluminum alloy. *Mater Trans* 2016;57(12):2104–9.
- [66] Silva CA, Rosa P, Martins P. Innovative testing machines and methodologies for the mechanical characterization of materials. *Exp Tech* 2016;40(2):569–81.
- [67] Dixit U, Joshi S, Davim JP. Incorporation of material behavior in modeling of metal forming and machining processes: a review. *Mater Des* 2011;32(7):3655–70.
- [68] Kocks UF, Argon AS, Ashby MF. *Thermodynamics and kinetics of slip*. Pergamon Press; 1975.
- [69] Butt M, Zubair M, Ul-Haq I. A comparative study of the stress relaxation in aged and un-aged high-purity aluminium polycrystals. *J Mater Sci* 2000;35(24):6139–44.
- [70] Bembalge O, Panigrahi S. Development and strengthening mechanisms of bulk ultrafine grained AA6063/SiC composite sheets with varying reinforcement size ranging from nano to micro domain. *J Alloys Compd* 2018;766:355–72.
- [71] Ross C, Roth JT. The effects of DC current on the tensile properties of metals. In: *ASME international mechanical engineering congress and exposition*, vol. 42347. ASME; 2005. p. 363–72.
- [72] Totten GE, MacKenzie DS. *Handbook of aluminum: vol. 1: physical metallurgy and processes*. CRC press; 2003.
- [73] Salandro WA, Bunget CJ, Mears L. A thermal-based approach for determining electroplastic characteristics. *Proc IME B J Eng Manufact* 2012;226(5):775–88.
- [74] Ruszkiewicz BJ, Mears L, Roth JT. Investigation of heterogeneous joule heating as the explanation for the transient electroplastic stress drop in pulsed tension of 7075-T6 aluminum. *J Manuf Sci Eng* 2018;140(9):091014.
- [75] Hudson A, Nelson RR. *University physics*. Philadelphia, USA: Saunders College Publishing; 1990.
- [76] Fraden J. *Handbook of modern sensors: physics, designs, and applications*. 4th. Newyork: Springer; 2010.
- [77] Kim M-J, Lee M-G, Hariharan K, Hong S-T, Choi I-S, Kim D, et al. Electric current-assisted deformation behavior of Al-Mg-Si alloy under uniaxial tension. *Int J Plast* 2017;94:148–70.
- [78] Estrin Y. Dislocation-density-related constitutive modeling. *Unified Constit Laws Plastic Deform* 1996;1:69–106.
- [79] Kocks U, Mecking H. Physics and phenomenology of strain hardening: the fcc case. *Prog Mater Sci* 2003;48(3):171–273.
- [80] Mecking H, Kocks U. Kinetics of flow and strain-hardening. *Acta Metall* 1981;29(11):1865–75.
- [81] Xiang S, Zhang X. Dislocation structure evolution under electroplastic effect. *Mater Sci Eng: A* 2019;761:138026.
- [82] Liu K, Dong X, Xie H, Wu Y, Peng F. Influence of pulsed current on deformation mechanism of AZ31B sheets during tension. *J Alloys Compd* 2016;676:106–12.
- [83] Siopis MS, Kinsey BL, Kota N, Ozdoganlar OB. Effect of severe prior deformation on electrical-assisted compression of copper specimens. *J Manuf Sci Eng* 2011;133(6):064502.
- [84] Huang K, Cayron C, Logé RE. The surprising influence of continuous alternating electric current on recrystallization behaviour of a cold-rolled aluminium alloy. *Mater Char* 2017;129:121–6.
- [85] Mishra S, Yadava M, Kulkarni KN, Gurao N. Stress relaxation behavior of an aluminium magnesium silicon alloy in different temper condition. *Mech Mater* 2018;125:80–93.
- [86] Livesay B, Donlin N, Garrison A, Harris H, Hubbard J. Dislocation based mechanisms in electromigration. In: *30th Annual Proceedings Reliability Physics* 1992. IEEE; 1992. p. 217–27.
- [87] Magargee J, Fan R, Cao J. Analysis and observations of current density sensitivity and thermally activated mechanical behavior in electrically-assisted deformation. *J Manuf Sci Eng* 2013;135(6):061022.
- [88] Ross CD, Irvin DB, Roth JT. Manufacturing aspects relating to the effects of direct current on the tensile properties of metals. *J Eng Mater Technol* 2007;129(2):342–7.
- [89] Magargee J, Morestin F, Cao J. Characterization of flow stress for commercially pure titanium subjected to electrically assisted deformation. *J Eng Mater Technol* 2013;135(4):041003.
- [90] Liu K, Dong X, Xie H, Peng F. Effect of pulsed current on the deformation behavior of AZ31B magnesium alloy. *Mater Sci Eng: A* 2015;623:97–103.
- [91] De Keijser TH, Langford JI, Mittemeijer EJ, Vogels ABP. Use of the Voigt function in a single-line method for the analysis of X-ray diffraction line broadening. *J Appl Crystallogr* 1982;15(3):308–14.
- [92] Sánchez-Bajo F, Ortiz AL, Cumbreira FL. Analytical formulation of the variance method of line-broadening analysis for voigtian X-ray diffraction peaks. *J Appl Crystallogr* 2006;39(4):598–600.
- [93] Dorofeev G, Streletskii A, Povstugar I, Protasov A, Elsukov E. Determination of nanoparticle sizes by X-ray diffraction. *Colloid J* 2012;74(6):675–85.
- [94] Dutta R. *Microstructural evolution during high-frequency post weld impact treatments for high-strength steels*. Ph.D. thesis. Delft University of Technology; 2015.
- [95] Wertheim G, Butler M, West K, Buchanan D. Determination of the Gaussian and Lorentzian content of experimental line shapes. *Rev Sci Instrum* 1974;45(11):1369–71.
- [96] Zhao J, Wang G-X, Dong Y, Ye C. Multiscale modeling of localized resistive heating in nanocrystalline metals subjected to electropulsing. *J Appl Phys* 2017;122(8):085101.
- [97] Kubin L, Estrin Y. Evolution of dislocation densities and the critical conditions for the Portevin-Le Chatelier effect. *Acta Metall Mater* 1990;38(5):697–708.
- [98] Andre D, Burlet T, Körkemeyer F, Gerstein G, Gibson J-L, Sandlöbes-Haut S, et al. Investigation of the electroplastic effect using nanoindentation. *Mater Des* 2019;183:108153.
- [99] Molotskii M, Kris R, Fleurov V. Internal friction of dislocations in a magnetic field. *Phys Rev B* 1995;51(18):12531.
- [100] Mishra G, Mohapatra S, Prusty S, Sharma MK, Chatterjee R, Singh S, et al. Magnetic properties of nanocrystalline  $\beta$ -SiC. *J Nanosci Nanotechnol* 2011;11(6):5049–53.